Acta Materialia 257 (2023) 119179

Contents lists available at ScienceDirect

Acta Materialia

journal homepage: www.elsevier.com/locate/actamat

Deformation mechanisms in an additively manufactured dual-phase eutectic high-entropy alloy

Jie Ren [a,1], Margaret Wu [b,1], Chenyang Li [c], Shuai Guan [a], Jiaqi Dong [d], Jean-Baptiste Forien [b], Tianyi Li [e], Katherine S. Shanks [f], Dunji Yu [g], Yan Chen [g], Ke An [g], Kelvin Y. Xie [d], Wei Chen [c], Thomas Voisin [b,*], Wen Chen [a,*]

[a] Department of Mechanical and Industrial Engineering, University of Massachusetts, Amherst, MA 01003, USA
[b] Materials Science Division, Lawrence Livermore National Laboratory, Livermore, CA 94550, USA
[c] Department of Mechanical, Materials, and Aerospace Engineering, Illinois Institute of Technology, Chicago, IL 60616, USA
[d] Department of Materials Science and Engineering, Texas A&M University, College Station, TX 77843, USA
[e] X-ray Science Division, Argonne National Laboratory, Argonne, IL 60439, USA
[f] Cornell High Energy Synchrotron Source, Ithaca, NY 14853, USA
[g] Neutron Scattering Division, Oak Ridge National Laboratory, Oak Ridge, TN 37831, USA

ARTICLE INFO

Keywords:
Additive manufacturing
High-entropy alloy
Nanolamellar structure
In-situ synchrotron X-ray diffraction
Mechanical property

ABSTRACT

Nanostructured metals and alloys often exhibit high strengths but at the expense of reduced ductility. Through harnessing the far-from-equilibrium processing conditions of laser powder-bed fusion (L-PBF) additive manufacturing, we develop a dual-phase nanolamellar structure comprised of FCC/$L1_2$ and BCC/B2 phases in a $Ni_{40}Co_{20}Fe_{10}Cr_{10}Al_{18}W_2$ eutectic high-entropy alloy (EHEA), which exhibits a combination of ultrahigh yield strength (>1.4 GPa) and large tensile ductility (~17%). The deformation mechanisms of the additively manufactured EHEA are studied via *in-situ* synchrotron X-ray diffraction and high-resolution transmission electron microscopy. The high yield strength mainly results from effective blockage of dislocation motion by the high density of lamellar interfaces. The refined nanolamellar structures and low stacking fault energy (SFE) promote stacking fault (SF)-mediated deformation in FCC/$L1_2$ nanolamellae. The accumulation of abundant dislocations and SFs at lamellar interfaces can effectively elevate local stresses to promote dislocation multiplication and martensitic transformation in BCC/B2 nanolamellae. The cooperative deformation of the dual phases, assisted by the semi-coherent lamellar interfaces, gives rise to the large ductility of the as-printed EHEA. In addition, we also demonstrate that post-printing heat treatment allows us to tune the non-equilibrium microstructures and deformation mechanisms. After annealing, the significantly reduced SFE and thicknesses of the FCC nanolamellae facilitate the formation of massive SFs. The dissolution of nano-precipitates in the BCC/B2 nanolamellae reduces spatial confinement and further promotes martensitic transformation to enhance work hardening. Our work provides fundamental insights into the rich variety of deformation mechanisms underlying the exceptional mechanical properties of the additively manufactured dual-phase nanolamellar EHEAs.

1. Introduction

Ultrahigh strength (gigapascal level) and large ductility are critical properties for developing lightweight components for applications that require structural reliability and energy efficiency. To achieve high strength, Hall-Petch strengthening by grain refinement has been widely adopted in many metallic materials. Unfortunately, this strategy often leads to an undesired loss in ductility [1–4]. This well-known strength-ductility tradeoff has been a longstanding challenge in structural materials [5,6]. In the past decades, materials with heterogeneities including bimodal, lamellar, gradient, nanodomain-dispersed, multi-phase, and hierarchical microstructural architectures have been developed to overcome the strength-ductility dilemma [7–10]. However, a critical challenge limiting their broad use for structural applications lies in their processing. Thus far, heterogeneous materials are mostly fabricated by thin-film deposition [11–13], surface mechanical treatment

* Corresponding authors.
E-mail addresses: voisin2@llnl.gov (T. Voisin), wenchen@umass.edu (W. Chen).
[1] These authors contributed equally to this work.

https://doi.org/10.1016/j.actamat.2023.119179
Received 24 March 2023; Received in revised form 25 June 2023; Accepted 21 July 2023
Available online 22 July 2023

[14,15], or multi-step thermo-mechanical treatment [16,17] which are not readily applicable to large-volume and intricate geometries.

Additive manufacturing (AM), or 3D printing, is an emerging technology that can directly produce complex and near-net-shape components. Metal 3D printing via laser powder-bed fusion (L-PBF) involves rapid and spatially-variable heating, melting, solidification and cooling cycles, and provides ample opportunities to tailor the microstructures and mechanical properties [18–20]. This has been demonstrated for a wide range of alloys such as stainless steels [21] and aluminum alloys [22,23]. However, successful printing by L-PBF depends not only on processing conditions but also largely on the intrinsic thermo-physical properties of the feedstock material. For example, laser absorptivity, vapor pressure, solidification range, and thermal expansion coefficient can dictate the presence of a variety of printing defects including porosity, loss of volatile alloying elements, hot cracking, accumulation of thermal residual stresses, or part distortion and delamination [20, 24–26]. These defects can deteriorate the mechanical properties and are thus detrimental to the performance and lifetime of additively manufactured metal alloys. Significantly, a majority of over 5500 existing alloys cannot be 3D-printed by L-PBF [23].

Eutectic high-entropy alloys (EHEAs) are a class of multi-principal element alloys often with dual-phase microstructures that provide a good combination of strength and ductility [16,27,28], excellent high-temperature performance, corrosion resistance, and wear resistance [29–31]. In addition, the narrow solidification range and the isothermal eutectic reaction are beneficial to mitigate hot cracking during solidification, which makes EHEAs promising candidates for AM. Considerable efforts have been devoted to investigating the feasibility of AM of EHEAs such as $AlCoCrFeNi_{2.1}$ [32–35], $Ni_{30}Co_{30}Cr_{10}Fe_{10}Al_{18}W_1Mo_1$ [36], $Ni_{32}Co_{30}Cr_{10}Fe_{10}Al_{18}$ [37], $Al_{0.75}CrFeNi$ [38] and $AlCrFe_2Ni_2$ [39]. These alloys have shown excellent mechanical properties including high strength and large ductility [35]. However, a fundamental understanding of their deformation mechanisms is critically needed.

$Ni_{40}Co_{20}Fe_{10}Cr_{10}Al_{18}W_2$ (at.%) is an EHEA that exhibits superior mechanical properties in the as-cast state due to its dual-phase B2/FCC microlamellar structure [40]. Here, we show that L-PBF can effectively refine the microstructure of $Ni_{40}Co_{20}Fe_{10}Cr_{10}Al_{18}W_2$ EHEA to form dual-phase nanolamellae comprised of alternating FCC/$L1_2$ and BCC/B2 phases. The as-printed $Ni_{40}Co_{20}Fe_{10}Cr_{10}Al_{18}W_2$ EHEA demonstrates doubled yield strength without a considerable sacrifice in ductility compared to the as-cast counterpart. We investigate the deformation mechanisms of the additively manufactured $Ni_{40}Co_{20}Fe_{10}Cr_{10}Al_{18}W_2$ using state-of-the-art characterization and modeling tools including *in-situ* synchrotron high-energy X-ray diffraction (HEXRD), transmission electron microscopy (TEM), and first-principles density functional theory (DFT) calculations. The achieved high ductility and sustained work hardening at high flow stresses arise from several sequentially activated deformation mechanisms. The refined nanolamellar structures and low stacking fault energy (SFE) promote abundant stacking faults (SFs) in the FCC/$L1_2$ nanolamellae. The accumulation of defects including dislocations and SFs at lamellar interfaces can effectively elevate local stresses, and subsequently trigger stress-induced martensitic transformation (SIMT) and dislocation nucleation in the BCC/B2 nanolamellae. The cooperative deformation of FCC/$L1_2$ and BCC/B2 nanolamellae, assisted by the semi-coherent lamellar interfaces, can effectively enhance the work hardening and thus contribute to the large ductility. In addition, we also demonstrate that post-printing heat treatment allows us to further tune the non-equilibrium microstructures and deformation mechanisms. After annealing at 900 °C for 1 h, the significantly reduced SFE and thicknesses of FCC nanolamellae facilitate the formation of massive SFs; the dissolution of nano-precipitates in the BCC/B2 nanolamellae reduces spatial confinement and further promotes martensitic transformation to enhance the work hardening. Our findings not only demonstrate that laser AM can be utilized to engineer metal alloys with outstanding mechanical properties, but also provide fundamental understanding of the deformation mechanisms that govern the exceptional mechanical properties of the additively manufactured dual-phase nanolamellar EHEAs.

2. Materials and methods

2.1. Materials processing

$Ni_{40}Co_{20}Fe_{10}Cr_{10}Al_{18}W_2$ (at.%) EHEA samples were printed by a commercial M290 (EOS GmbH, Germany) L-PBF machine equipped with a 400-W Yb-fiber laser. The laser beam was focused through an F-theta lens to a diameter of 100 μm. Gas-atomized $Ni_{40}Co_{20}Fe_{10}Cr_{10}Al_{18}W_2$ (at.%) EHEA powders with particle sizes ranging from 15 μm to 53 μm were used for printing (Supplementary Fig. S1). The processing chamber was filled with high-purity argon and the oxygen content was maintained below 1000 ppm during printing. A 4140 alloy steel printing substrate was used and pre-heated to 150 °C to minimize thermal residual stresses and improve surface adhesion. A bi-continuous scan strategy with 5 mm wide stripes and 67° inter-layer rotation was applied to reduce thermal residual stresses. We printed 35 mm (length) × 10 mm (width) × 2 mm (height) EHEA plates with a relative density higher than 99.5%. Our optimized parameters are: laser power of 300 W, scan speed of 900 mm/s, hatching spacing of 0.08 mm and layer thickness of 0.04 mm. To study the effects of post-printing heat treatment on microstructural evolution and mechanical properties, the as-printed samples were subsequently annealed at 900 °C for 1 h in a muffle furnace followed by water quenching.

2.2. Mechanical testing

Dog-bone-shaped tensile specimens with nominal gauge dimensions of 8 mm (length) × 2 mm (width) × 1 mm (thickness) were cut from the rectangular plates by electrical discharge machining (EDM) and polished to a metallurgical grit of 1200 SiC paper. The tensile direction is perpendicular to the build direction. Quasi-static tensile tests were conducted on an Instron 5969 universal testing machine at a strain rate of 2×10^{-4} /s. The strain was measured by an Instron non-contact AVE2 video extensometer with a displacement resolution of 0.5 μm. Three tests were repeated for each type of sample.

2.3. Material characterization

The density of the as-printed samples was measured by an AccuPyc II 1340 gas pycnometer. The phase constitution of the EHEA powders was verified with an X-ray diffractometer (XRD, PANalytical X'Pert) using a Cu target, a voltage of 45 kV, a current of 40 mA, scanning angles ranging from 20° to 100°, a step size of 0.005°, and a speed of 5 s/step. Scanning electron microscopy (SEM) imaging was conducted in an FEI Magellan 400 microscope. Electron backscatter diffraction (EBSD) was performed at an accelerating voltage of 20 kV in a ThermoFisher Apreo™ SEM equipped with an EDAX Velocity EBSD camera. EBSD maps were collected using a step size of 50 nm and the data was analyzed using EDAX Orientation Imaging Microscopy (OIM)™ software. EBSD samples were polished using 20 nm colloidal silica suspension. Disk-shaped TEM specimens with a diameter of 3 mm were punched out of mechanically grounded ~100 μm-thick foils, and subsequently electropolished in a 60% methanol, 35% butanol, 5% perchloric acid solution at approximately −40 °C and 20 V/16 mA using a Struers Tenupol twin-jet polisher. TEM was conducted in an FEI 80–300 Titan microscope at 300 kV equipped with a four-detector energy dispersive X-ray spectroscopy (EDX) system, ChemiSTEM™. Precession electron diffraction (PED)-based crystal orientation mapping in the TEM was performed using the Topspin setup from Nanomegas. Lamellar thickness distributions were measured on TEM images with the ImageJ software. Approximately 200 lamellae were analyzed to ensure good statistics.

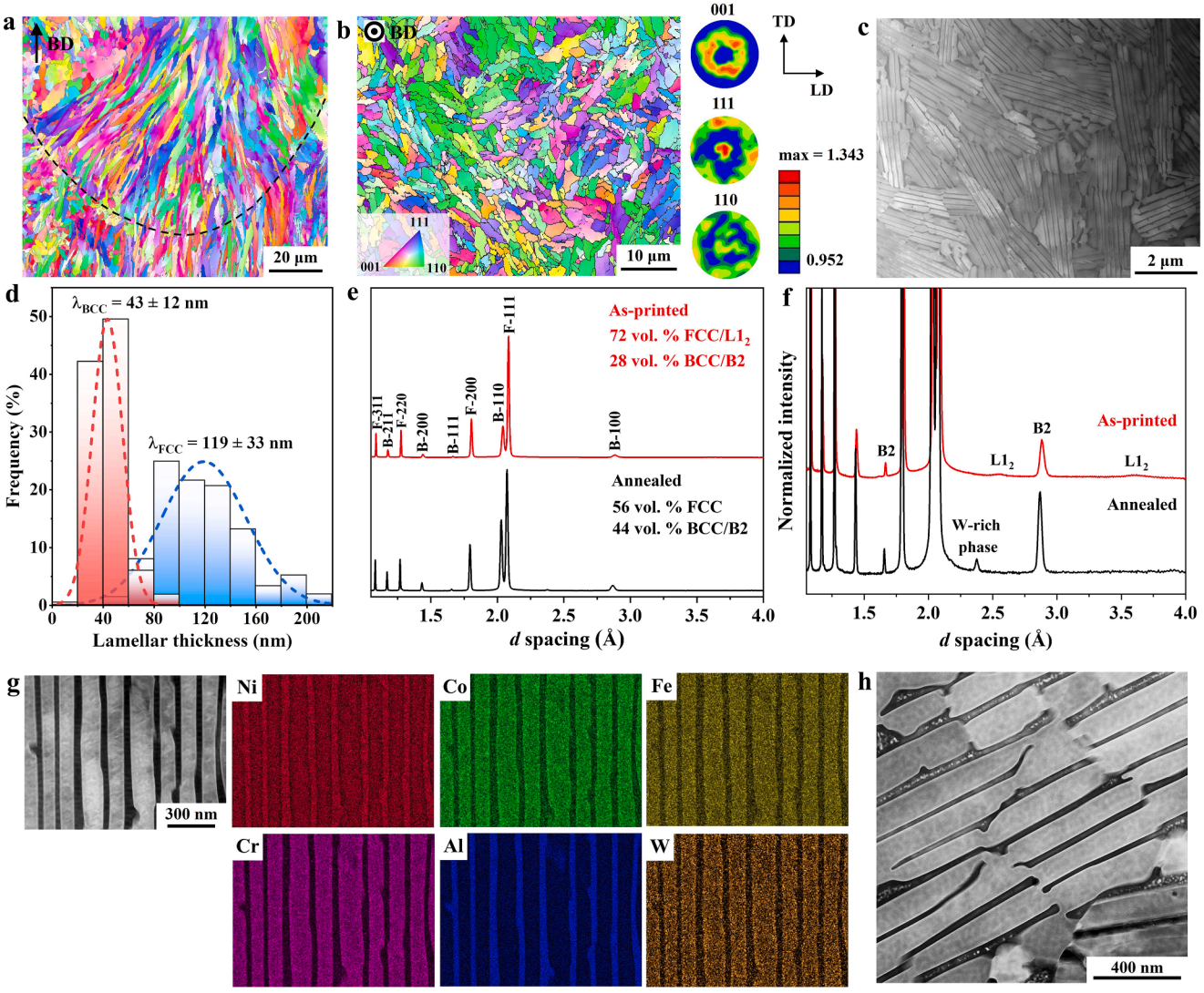

Fig. 1. Hierarchical microstructures of the as-printed $Ni_{40}Co_{20}Fe_{10}Cr_{10}Al_{18}W_2$ EHEA. (a) EBSD inverse pole figure (IPF) map of the side-view cross section of the as-printed $Ni_{40}Co_{20}Fe_{10}Cr_{10}Al_{18}W_2$ EHEA. The melt pool boundary is illustrated by the black dash line. (b) EBSD IPF map of the top-view cross section of the as-printed $Ni_{40}Co_{20}Fe_{10}Cr_{10}Al_{18}W_2$ EHEA and the corresponding 001, 110, 111 pole figures of FCC/L1$_2$ phase. Note that the BCC/B2 nanolamellae are under-indexed by EBSD due to their small thicknesses of ~43 nm. (c) High-angle annular dark-field (HAADF)-STEM micrograph showing the microscale eutectic colonies with nanolamellae embedded in them. (d) BCC/B2 and FCC/L1$_2$ lamellar thickness distributions in the as-printed $Ni_{40}Co_{20}Fe_{10}Cr_{10}Al_{18}W_2$ EHEA. (e) HEXRD spectra of the as-printed and annealed $Ni_{40}Co_{20}Fe_{10}Cr_{10}Al_{18}W_2$ EHEAs. (f) Enlarged diffraction spectra showing the existence of B2 and L1$_2$ superlattice reflections. (g) STEM-EDX elemental maps of the as-printed $Ni_{40}Co_{20}Fe_{10}Cr_{10}Al_{18}W_2$ EHEA. (h) HAADF-STEM image showing some nano-precipitates sparsely distributed in the relatively coarser BCC/B2 nanolamellae of the as-printed $Ni_{40}Co_{20}Fe_{10}Cr_{10}Al_{18}W_2$ EHEA.

2.4. *In-situ* synchrotron high-energy X-ray diffraction

In-situ synchrotron high-energy X-ray diffraction tensile tests were performed at the Advanced Photon Source (APS) at the Argonne National Laboratory (ANL) and Cornell High Energy Synchrotron Source (CHESS). CHESS was used to perform preliminary studies on annealed samples (see Supplementary note) and these samples were further studied more thoroughly at APS. At APS, the dog-bone-shaped tensile specimen (gauge length: 10.16 mm, width: 3.175 mm, thickness: 0.75 mm) was mounted on a stress rig implemented at the sample holder with X-Y-Z translation. Two-dimensional (2D) X-ray diffraction patterns were collected in transmission mode at the gauge section of the tensile specimen with a PerkinElmer amorphous silicon-based area detector which was positioned 1200 mm behind the sample. Diffraction patterns were collected with an exposure time of 2 s during tensile deformation and the nominal strain rate was ~2.5×10^{-4} /s. The 2D diffraction patterns were integrated along specified azimuth angles over a range of ± 5° to obtain one-dimensional (1D) diffraction spectra using GSAS-II software [41]. The Pseudo-Voigt function was used for single-peak fitting to extract the peak position, integrated intensity, and full width at half maximum (FWHM). Standard CeO_2 and LaB_6 powders were used to calibrate the sample-to-detector distance and the instrumental broadening.

Crystal lattice spacings of specific {*hkl*} crystallographic reflections were converted from the diffraction angle θ following Bragg's law. The elastic lattice strain (ε_{hkl}) was calculated by:

$$\varepsilon_{hkl} = \left(d_{hkl} - d_{0,hkl}\right)/d_{0,hkl} \quad (1)$$

where d_{hkl} and $d_{0,hkl}$ refer to the crystal lattice spacings of {*hkl*} reflections under an applied load and the load-free state, respectively.

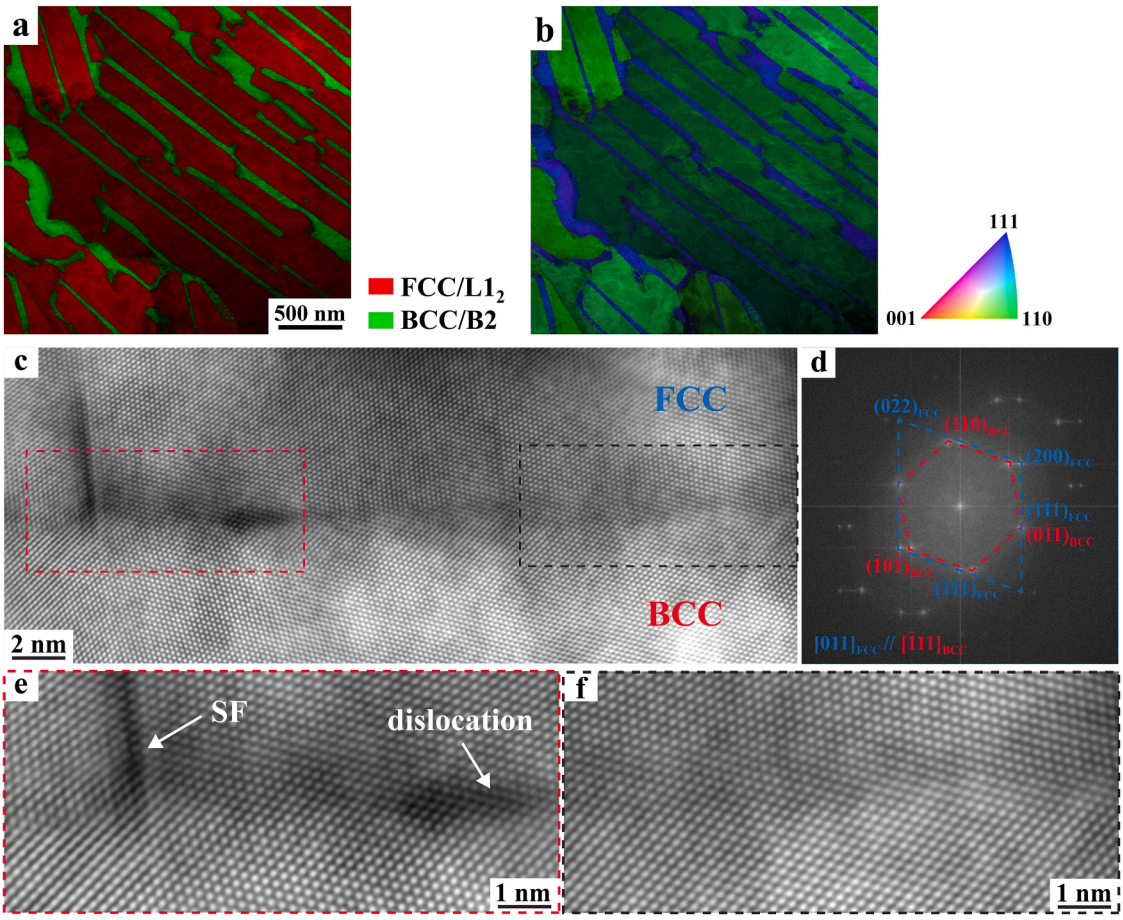

Fig. 2. (a) PED phase map and (b) IPF map imposed on the image quality map of the nanolamellar structures of the as-printed $Ni_{40}Co_{20}Fe_{10}Cr_{10}Al_{18}W_2$ EHEA. (c) HRTEM micrograph showing the BCC/B2 and FCC/$L1_2$ interface of the as-printed $Ni_{40}Co_{20}Fe_{10}Cr_{10}Al_{18}W_2$ EHEA. (d) The corresponding FFT diffractogram of the phase interface showing the favorable K-S orientation relationship between BCC/B2 and FCC/$L1_2$ phases. (e) The enlarged HRTEM micrograph of the red boxed region in (c) showing the interface dislocation and SF. (f) The enlarged HRTEM micrograph of the defect-free region (black boxed region in (c)) (For interpretation of the references to color in this figure legend, the reader is referred to the web version of this article).

3. Results

3.1. Microstructure and phase analysis

Strong temperature gradients (10^6–10^7 K/m) and high cooling rates (10^5–10^7 K/s) during L-PBF [42] result in non-equilibrium hierarchical microstructures in the as-printed $Ni_{40}Co_{20}Fe_{10}Cr_{10}Al_{18}W_2$ EHEA (Fig. 1). From the side view, it is seen that elongated eutectic colonies with different crystallographic orientations grow along the direction of the thermal gradient, which is normal to the local melt pool boundary (Fig. 1a). When cross-sectioned, these eutectic colonies exhibit an almost equiaxed morphology with an average diameter of 2.5 ± 1.2 μm (top view, Fig. 1b). Pole figures show a small maximum multiple randomness of uniform distribution (m.r.d) value of 1.343, indicating a nearly random texture of the as-printed $Ni_{40}Co_{20}Fe_{10}Cr_{10}Al_{18}W_2$ EHEA. TEM and HEXRD characterizations reveal that alternating FCC and BCC-based lamellae with a respective thickness of 119 ± 33 nm and 43 ± 12 nm are embedded inside the microscale eutectic colonies (Fig. 1c-f). The average interlamellar spacing ($\lambda \approx 162$ nm) is ~5 times smaller than that in the as-cast counterpart ($\lambda \approx 820$ nm) [40]. Notably, $L1_2$ and B2 superlattice reflections can be observed by HEXRD (Fig. 1e-f) and further confirmed by neutron diffraction, which allows probing a much larger volume of sample material (Supplementary Fig. S2). These results indicate the existence of ordered structures besides the FCC and BCC solid solutions. Rietveld refinement of the HEXRD spectrum shows that the volume fractions of FCC/$L1_2$ and BCC/B2 phases are ~72% and ~28%, respectively (Fig. 1e). Scanning TEM (STEM)-EDX mapping reveals that BCC/B2 lamellae are rich in Al and Ni, whereas FCC/$L1_2$ lamellae are enriched by Co, Cr, Fe, and W (Fig. 1g). Some Cr- and W-rich BCC nano-precipitates are sparsely distributed in BCC/B2 nanolamellae, especially in the relatively coarser ones (Fig. 1h and Supplementary Fig. S3). It is well documented that the Cr-rich BCC nano-precipitates are present inside the B2 lamellae in the as-cast [43] and thermo-mechanically treated [44] $AlCoCrFeNi_{2.1}$ EHEAs. Meanwhile, $L1_2$ structures appear as spherical, nanoscale inclusions embedded within FCC nanolamellae, as depicted by TEM dark-field (DF) imaging (Supplementary Fig. S4). The strong elemental partitioning and existence of ordered structures and nano-precipitates in $Ni_{40}Co_{20}Fe_{10}Cr_{10}Al_{18}W_2$ EHEA during rapid solidification of L-PBF stand in contrast to the largely suppressed atomic diffusion and chemical ordering in other additively manufactured EHEAs such as $AlCoCrFeNi_{2.1}$ [35]. The above findings manifest the distinct diffusion and precipitation kinetics in different EHEAs upon rapid solidification.

We further characterized the structure and orientation of the lamellar interfaces by PED. Fig. 2a shows the continuously alternating FCC/$L1_2$ and BCC/B2 nanolamellar structures. The $<011>_{FCC}$ // $<111>_{BCC}$ and $\{111\}_{FCC}$ // $\{011\}_{BCC}$ Kurdjumov-Sachs (K-S) orientation relationship is found between the dual phases (Fig. 2b). Fig. 2c shows the corresponding semi-coherent interface using high-resolution TEM (HRTEM). The fast Fourier transform (FFT) diffractogram in Fig. 2d confirms the K-S orientation relationship. This type of phase interface is known to be energetically more favorable with a crystal

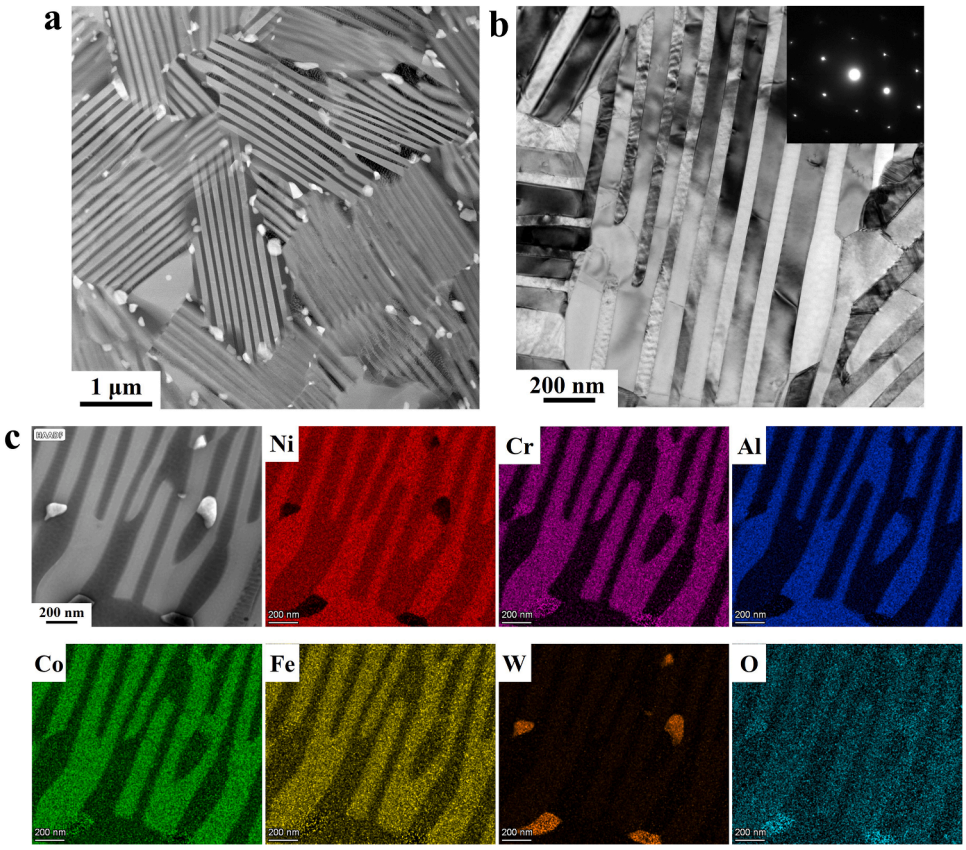

Fig. 3. (a) HAADF-STEM and (b) Bright-field (BF) TEM images showing the microscale eutectic colonies and the nanoscale lamellar structures of the annealed $Ni_{40}Co_{20}Fe_{10}Cr_{10}Al_{18}W_2$ EHEA. The inset shows the SAED pattern of an FCC lamella. No superlattice spots are observed, suggesting that only disordered FCC phase is present. (c) STEM-EDX elemental maps of the annealed $Ni_{40}Co_{20}Fe_{10}Cr_{10}Al_{18}W_2$ EHEA.

Table 1
Chemical compositions (measured by STEM-EDX) and volume fractions of different phases in the as-printed and annealed $Ni_{40}Co_{20}Fe_{10}Cr_{10}Al_{18}W_2$ EHEAs.

Sample condition	Phase	Volume fraction (%)	Element (at.%)					
			Al	Cr	Fe	Co	Ni	W
Nominal	Nominal	–	18	10	10	20	40	2
As-printed	FCC/$L1_2$	72	10.8 ± 1.2	12.0 ± 1.0	11.7 ± 0.8	22.5 ± 1.2	40.2 ± 2.1	2.8 ± 0.5
	BCC/B2	28	26.7 ± 1.1	4.1 ± 0.5	7.4 ± 0.6	15.6 ± 0.6	45.0 ± 1.2	1.2 ± 0.2
Annealed	FCC	56	9.0 ± 0.5	15.4 ± 0.5	13.4 ± 0.5	26.2 ± 0.6	34.0 ± 0.7	2.0 ± 0.1
	BCC/B2	44	34.3 ± 0.9	2.8 ± 0.2	6.3 ± 0.4	11.6 ± 0.5	44.7 ± 0.9	0.3 ± 0.0

lattice mismatch periodically compensated by misfit dislocations or SFs [45] as observed in Fig. 2c and e. Notably, Fig. 2f shows that lattice coherency can be maintained over long distances (> 10 nm) without misfit dislocations. HEXRD results suggest that the lattice parameters of FCC/$L1_2$ and BCC/B2 phases are 3.59082 ± 0.00004 Å and 2.87126 ± 0.00010 Å, respectively, corresponding to a lattice misfit of 2.09%. Such semi-coherent interfaces with the small misfit strain can effectively enhance the strength and ductility of the additively manufactured dual-phase nanolamellar EHEA, to be discussed later.

To elucidate the effect of non-equilibrium solidification features on the deformation mechanisms of the additively manufactured $Ni_{40}Co_{20}Fe_{10}Cr_{10}Al_{18}W_2$ EHEA, we also investigated the microstructure and mechanical behavior of the material after post-printing heat treatment as a comparison. As shown in Fig. 3a and b, annealing at 900 °C for 1 h does not significantly change the colony size but removes most printing-induced dislocations. The average thickness of FCC-based lamellae decreases by ~20% (from 119 nm to 95 nm), whereas the average thickness of BCC-based lamellae increases by ~46% (from 43 nm to 63 nm), likely a result of interface migration at the elevated temperature. Interestingly, HEXRD measurements reveal that the annealed $Ni_{40}Co_{20}Fe_{10}Cr_{10}Al_{18}W_2$ is mainly composed of disordered FCC (56 vol.%) and a mixture of disordered and ordered BCC phases (44 vol.%) (Fig. 1e-f). The fully disordered nature of FCC nanolamellae accompanied by the annihilation of ordered $L1_2$ nanostructures after annealing is also indicated by the absence of extra superlattice spots in the selected area electron diffraction (SAED) pattern in Fig. 3b. Compared to the as-printed sample, the volume fraction of FCC phase decreases from 72% to 56%, whereas the volume fraction of BCC/B2 phase increases from 28% to 44%. Moreover, stronger elemental partitioning between dual phases is observed in the annealed $Ni_{40}Co_{20}Fe_{10}Cr_{10}Al_{18}W_2$ due to accelerated atomic diffusion at the elevated temperature (Fig. 3c and Table 1). We also note W-rich precipitates depleted in Ni and Al at the colony boundaries after annealing (Fig. 3a and c). Due to the low volume fraction and the large average spacing of these precipitates, their contribution to the strengthening is expected to be insignificant.

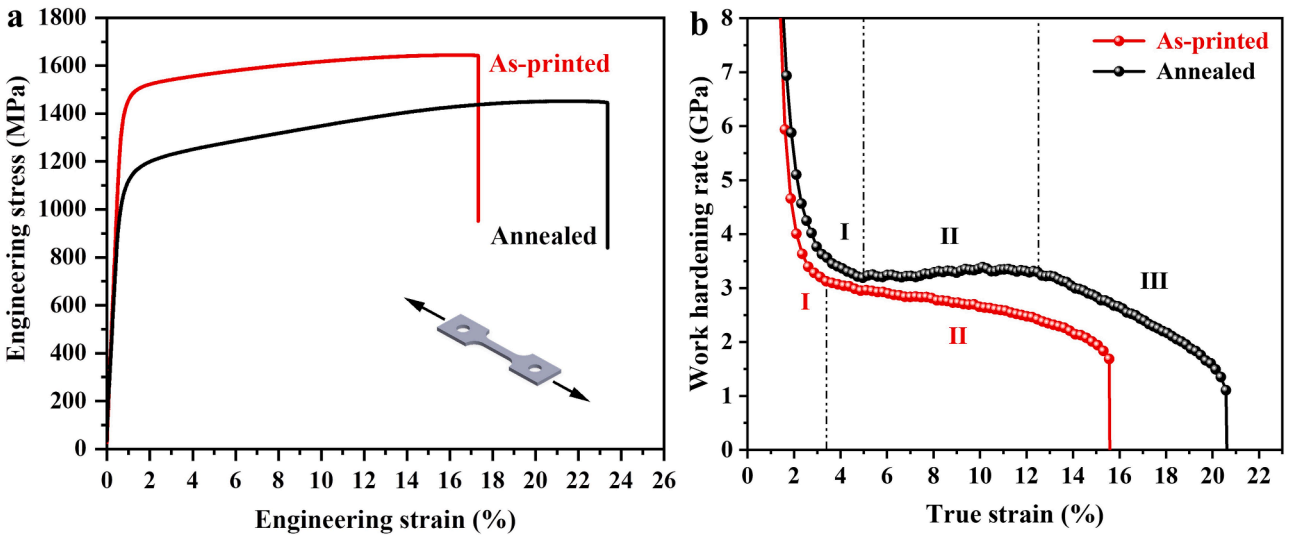

Fig. 4. (a) Engineering stress-strain curves of the as-printed and annealed $Ni_{40}Co_{20}Fe_{10}Cr_{10}Al_{18}W_2$ EHEAs. (b) Work hardening rate versus true strain of the as-printed and annealed $Ni_{40}Co_{20}Fe_{10}Cr_{10}Al_{18}W_2$ EHEAs.

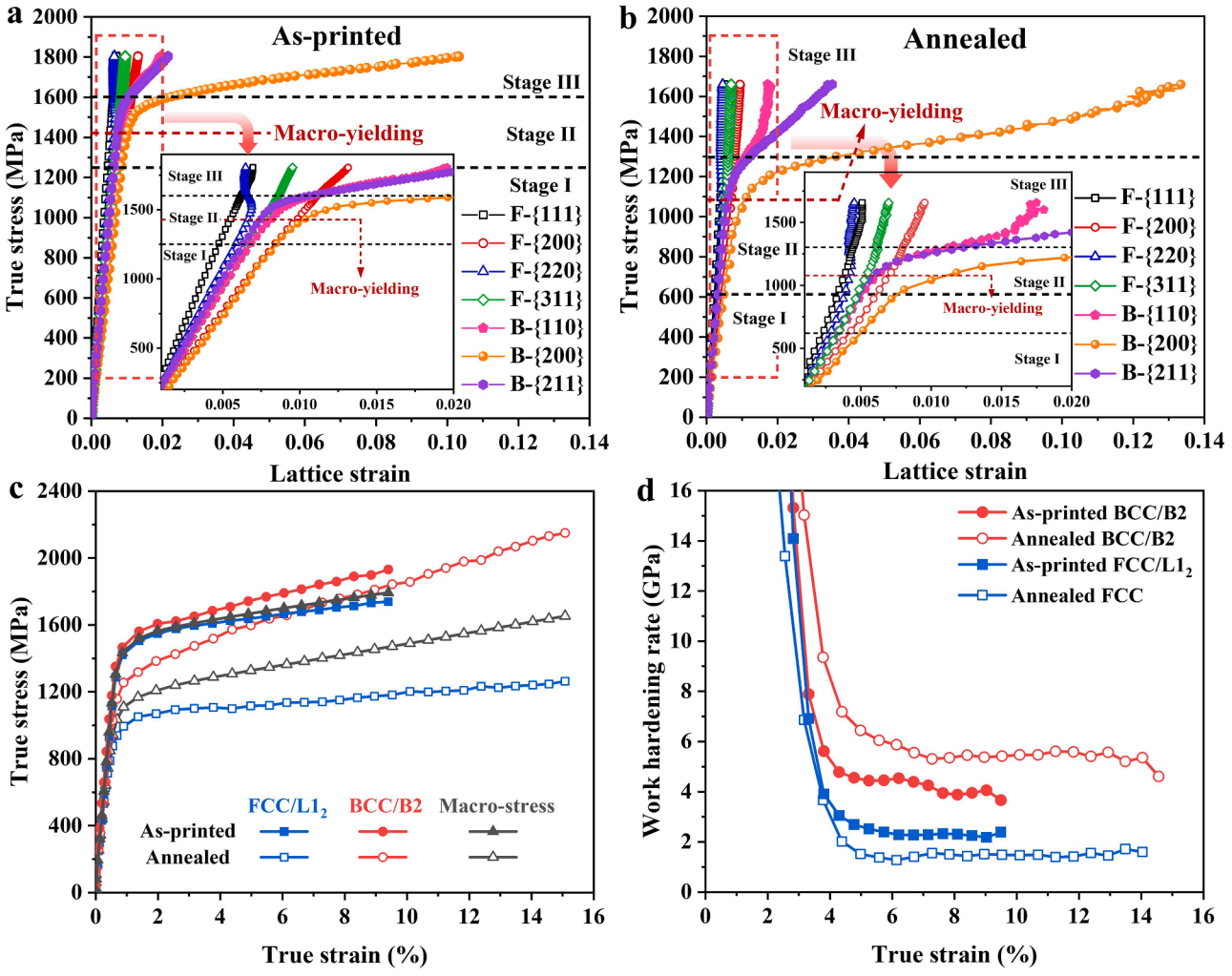

Fig. 5. (a, b) Lattice strain evolutions of FCC/$L1_2$ and BCC/B2 phases along LD of the as-printed and annealed $Ni_{40}Co_{20}Fe_{10}Cr_{10}Al_{18}W_2$ EHEAs, respectively. The stress for macro-yielding refers to the 0.2%-offset yield strength of the bulk sample. (c) Stress partitioning in FCC/$L1_2$ and BCC/B2 phases during tensile loading. (d) Work hardening rate versus true strain of FCC/$L1_2$ and BCC/B2 phases during tensile loading.

3.2. Mechanical properties

Fig. 4a shows the representative engineering tensile stress-strain curves of the as-printed and annealed $Ni_{40}Co_{20}Fe_{10}Cr_{10}Al_{18}W_2$ EHEAs. The as-printed sample exhibits an ultrahigh yield strength (σ_{YS}) of 1.42 ± 0.01 GPa, about twofold that of the as-cast counterpart (0.75 GPa) [40], and an ultimate tensile strength (σ_{UTS}) of 1.64 ± 0.01 GPa. The as-printed sample also displays a large uniform elongation of ~16.5%. After annealing at 900 °C for 1 h, the uniform elongation of L-PBF $Ni_{40}Co_{20}Fe_{10}Cr_{10}Al_{18}W_2$ EHEA increases to ~23%, while σ_{YS} and σ_{UTS} decrease to ~ 1.08 ± 0.01 GPa and 1.46 ± 0.01 GPa, respectively. Fig. 4b illustrates the work hardening rate of the as-printed and annealed $Ni_{40}Co_{20}Fe_{10}Cr_{10}Al_{18}W_2$ EHEAs as a function of true strain (ε_T). Both samples exhibit a steep decrease in working hardening rate in stage I, indicating the prominent role of dislocation slips at the early stage of plastic deformation [46]. With further increase in ε_T, the work hardening rate of the as-printed sample gradually decreases, but still retains above 1.5 GPa prior to plastic instability. For the as-printed sample with higher strength, the sustained work hardening capability (σ_{UTS} - σ_{YS} = 0.23 GPa, σ_{YS}/σ_{UTS} = 0.86) at high flow stresses gives rise to the large uniform elongation. Notably, the annealed sample exhibits a small hump after stage I. The gradual increase in work hardening rate until $\varepsilon_T \approx 12.5\%$ in stage II can be attributed to the prevailing role of extra deformation carriers, such as SFs and martensitic transformation (see discussion later). Finally, the work hardening rate of the annealed sample gradually decreases in stage III, which suggests that the phase transformation tends to saturate.

3.3. In-situ synchrotron HEXRD under tension

3.3.1. Real-time load partitioning behavior

Deformation mechanisms of the as-printed and annealed $Ni_{40}Co_{20}Fe_{10}Cr_{10}Al_{18}W_2$ EHEAs were investigated using *in-situ* synchrotron HEXRD measurements under uniaxial tension. This technique can provide unique insights into crystallographic lattice strain evolution and stress partitioning between different phases. For the as-printed and annealed $Ni_{40}Co_{20}Fe_{10}Cr_{10}Al_{18}W_2$ EHEAs, changes in elastic lattice strain ε_{hkl} along the loading direction (LD) as a function of the applied stress for different {*hkl*} crystallographic plane families in FCC/$L1_2$ and BCC/B2 phases are shown in Fig. 5a and b, respectively. Three stages can be observed. In stage I, lattice strain increases linearly with the applied stress for both as-printed and annealed samples, evident of purely elastic deformation. Note that the applied stress versus lattice strain curves for different crystallographic plane families exhibit different slopes due to their different diffraction elastic constant E_{hkl} [47,48]. In stage II, FCC plane families yield progressively while BCC plane families remain elastic. For the as-printed sample, when the applied stress exceeds ~1250 MPa, the FCC-{220} (denoted as F-{220} hereafter) plane family first deviates from linearity and shifts upward, indicating plastic deformation initiated in FCC/$L1_2$ nanolamellae oriented with a {220} plane perpendicular to LD. Meanwhile, the F-{200} plane family turns downward, which results from load shedding from the plastic F-{220} plane family. For the annealed sample, this same F-{220} plane family yields at a much lower stress of ~600 MPa. The softening of FCC phase is likely due to annihilation of pre-existing dislocations and dissolution of the ordered $L1_2$ nanostructures after heat treatment (Fig. 3b). Subsequently, F-{311}, {200}, and {111} plane families yield gradually for both as-printed and annealed samples, as shown by the increased slope of applied stress versus lattice strain. For better interpretation, we also plotted the deviation of elastic lattice strain from the initial linear range (Supplementary Fig. S5), which is defined as the intergranular/-interphase strain by the following equation:

$$\Delta\varepsilon_{hkl} = \varepsilon_{hkl} - \sigma_{applied}/E_{hkl} \quad (2)$$

where $\sigma_{applied}$ is the applied tensile stress. The progressive yielding of FCC/$L1_2$ phase transfers stress to the harder BCC/B2 phase, where larger elastic strains develop. In stage III, BCC/B2 phase plastically deforms in both as-printed and annealed samples with strong work hardening. Except for the F-{220} reflection, ε_{hkl} of other plane families increase with the applied stress, which is mainly contributed by the work hardening in each phase. The increase in lattice strain of BCC/B2 plane families is much faster than that of FCC/$L1_2$ plane families, suggesting BCC/B2 phase bears higher stresses than FCC/$L1_2$ phase during plastic deformation. Interestingly, B-{200} plane family develops an abnormally large lattice strain as high as 0.10 and 0.13 in the as-printed and annealed $Ni_{40}Co_{20}Fe_{10}Cr_{10}Al_{18}W_2$ EHEAs, respectively, and the origin will be discussed later.

In-situ HEXRD measurements also allow for quantitatively estimating phase-specific stresses σ_{phase} using the Hooke's law [49]:

$$\sigma_{phase} = E_{phase} \times \varepsilon_{phase} \quad (3)$$

where ε_{phase} is the phase strain along LD and E_{phase} is the Young's modulus of individual phase. Because the F-{311} plane family shows the least intergranular/interphase strain and has the diffraction elastic constant closest to the Young's modulus of bulk material [50,51], it was selected to represent the global behavior of FCC/$L1_2$ phase. Considering the possible phase transformations associated with BCC/B2 phase [50,52,53] (and also see Section 3.3.4), we did not directly calculate the phase stress for BCC/B2 phase from lattice strains. Instead, BCC/B2 phase stress was back-calculated based on a rule of mixture:

$$\sigma_{BCC} = \left(\sigma_{applied} - f_{FCC}\sigma_{FCC}\right)/f_{BCC} \quad (4)$$

where $\sigma_{applied}$ is the applied stress, σ_{FCC} and σ_{BCC} are the phase stress of FCC/$L1_2$ and BCC/B2 phases, respectively, and f_{FCC} and f_{BCC} are the volume fraction of FCC/$L1_2$ and BCC/B2 phases, respectively. Calculated phase stresses are presented in Fig. 5c, which shows that after macroscopic yielding the BCC/B2 phase exhibits higher work hardening rates compared to FCC/$L1_2$ phase. Apparently, the difference in work hardening rate between BCC/B2 and FCC/$L1_2$ phases becomes more significant after annealing (Fig. 5d).

3.3.2. Dislocation density evolution during deformation

To unveil the origin of the high work hardening rate in our additively manufactured dual-phase nanolamellar $Ni_{40}Co_{20}Fe_{10}Cr_{10}Al_{18}W_2$ EHEAs, we first examined the evolution of dislocation density. The as-printed $Ni_{40}Co_{20}Fe_{10}Cr_{10}Al_{18}W_2$ EHEA has a high initial dislocation density in the FCC/$L1_2$ phase of $\rho_{FCC} \approx 1.2 \times 10^{14}$ /m^2 based on Modified Williamson-Hall (MWH) line profile analysis (Supplementary Fig. S6a), which likely originates from the thermal residual stresses during rapid cooling of the L-PBF process [54]. After annealing, FWHMs of FCC peaks before deformation are negligibly small (near zero) after subtraction of the instrumental broadening (Supplementary Fig. S6b), indicating only few dislocations are present. This result agrees well with the TEM observation (Fig. 3b). Since BCC/B2-{200} diffraction peak along LD is affected by phase transformation during deformation (see Section 3.3.4), we do not have sufficient high-quality data points for MWH fitting to precisely quantify the dislocation density in BCC/B2 phase. Therefore, the dislocation density evolution during deformation is qualitatively analyzed by comparing the FWHM (after subtracting the instrumental broadening) of the representative first-order reflections of FCC/$L1_2$-{111} and BCC/B2-{110} along LD since these crystallographic reflections are typically unaffected by phase transformation. Based on MWH theory [52,55,56], FWHM is related to dislocation density ρ by the following equation:

$$\rho \sim (\Delta K/K)^2 \Big/ b^2\overline{C} \quad (5)$$

where $K = 2\sin\theta/\lambda$, in which θ and λ are the diffraction angle and the wavelength, respectively; ΔK is the FWHM in K space and defined as $\Delta K = 2\cos\theta(\Delta\theta)/\lambda$, b the magnitude of Burgers vector, $\overline{C}$ the average

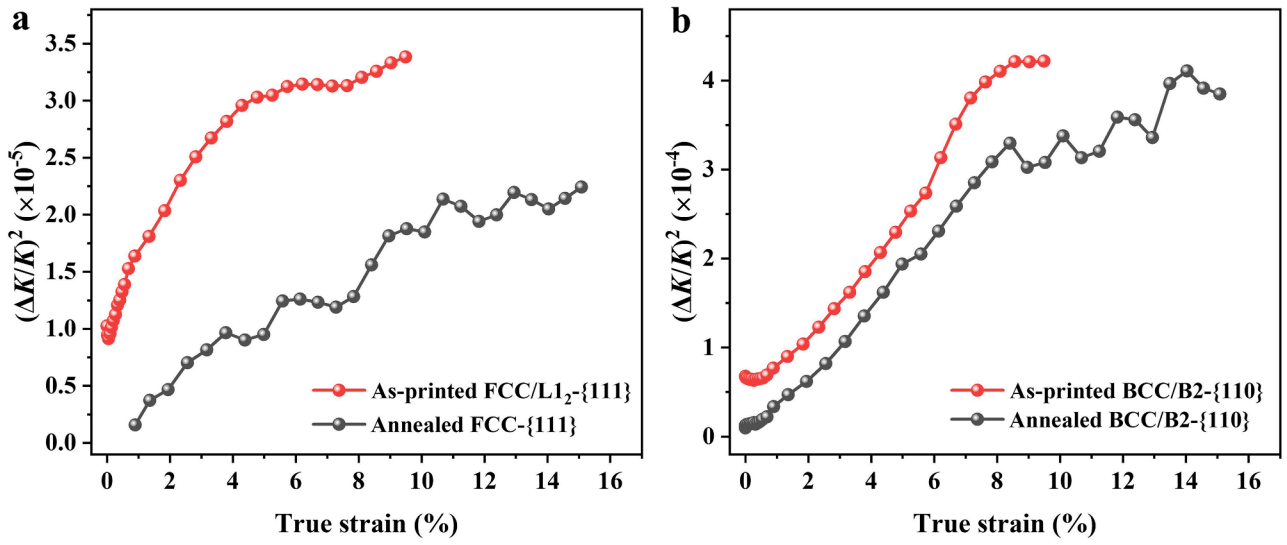

Fig. 6. (a) Evolutions of $(\Delta K/K)^2$ of FCC/L1$_2$-{111} versus true strain of the as-printed and annealed $Ni_{40}Co_{20}Fe_{10}Cr_{10}Al_{18}W_2$ EHEAs during tensile loading. (b) Same as (a) except for BCC/B2-{110} reflection.

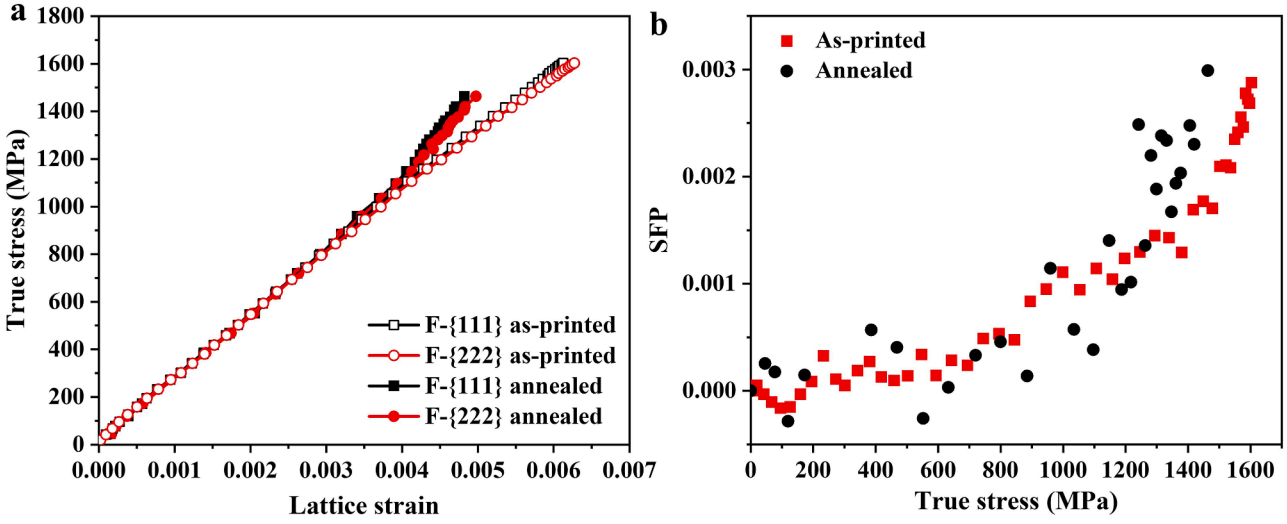

Fig. 7. (a) Lattice strain evolutions of the first order F-{111} and the second order F-{222} reflections of the as-printed and annealed $Ni_{40}Co_{20}Fe_{10}Cr_{10}Al_{18}W_2$ EHEAs during tensile loading. Since the B-{110} and {220} reflections develop large elastic lattice strains and significant peak broadening at large strains, these two peaks almost merge into the F-{111} and {222} peaks, respectively. This will introduce large uncertainties for peak deconvolution. So we did not study the lattice strain evolutions of F-{111} and {222} reflections for the as-printed sample as $\sigma_T > 1600$ MPa and for the annealed sample as $\sigma_T > 1460$ MPa. (b) SFP evolutions of the as-printed and annealed $Ni_{40}Co_{20}Fe_{10}Cr_{10}Al_{18}W_2$ EHEAs during tensile loading.

dislocation contrast factor associated with the dislocation character (edge or screw). As shown in Fig. 6a, for the as-printed sample, ρ_{FCC} increases continuously up to $\varepsilon_T \approx 5\%$, after which ρ_{FCC} saturates and increases again at $\varepsilon_T \approx 8\%$. For the annealed sample, ρ_{FCC} continuously increases throughout the entire uniform plastic deformation regime. On the other hand, dislocation density in BCC/B2 phase (ρ_{BCC}) of the as-printed sample increases up to $\varepsilon_T \approx 8\%$, after which it stabilizes (Fig. 6b). Note that the increase in ρ_{BCC} becomes markedly faster at $\varepsilon_T \approx 6\%$. In the annealed sample, the increase in ρ_{BCC} is continuous up to $\varepsilon_T \approx 8\%$, similar to the as-printed sample. Beyond that, the increase in ρ_{BCC} slows down.

3.3.3. *Stacking fault probability evolution during deformation*

SF formation is an important deformation mechanism in FCC structures with low SFE. Stacking fault probability (SFP), defined as the probability of finding a fault between any two layers in the FCC stacking sequence [57], can be measured via HEXRD analysis [58,59]. In principle, {111} and {222} planes undergo the same amount of elastic strain during macroscopic deformation, but when SFs are created, they cause the corresponding diffraction peaks to shift in opposite directions. As a result, SFP can be calculated from the difference between ε_{111} and ε_{222} [60]:

$$\mathrm{SFP} = \frac{32\pi}{3\sqrt{3}}(\varepsilon_{222} - \varepsilon_{111}) \tag{6}$$

As shown in Fig. 7a, ε_{111} and ε_{222} as a function of true stress (σ_T) overlap well in the elastic deformation stage. However, above 1200 MPa, a split between ε_{111} and ε_{222} becomes noticeable. Correspondingly, Fig. 7b shows the SFP as a function of σ_T. SFP for both as-printed and annealed samples are on the order of 10^{-3}, which is typical for materials undergoing SF formation rather than mechanical twinning [61]. For the as-printed sample, SFP increases rather continuously with the applied stress and reaches 2.9×10^{-3} at 1600 MPa. For the annealed sample, SFP remains more or less constant up to 1100 MPa, above which it

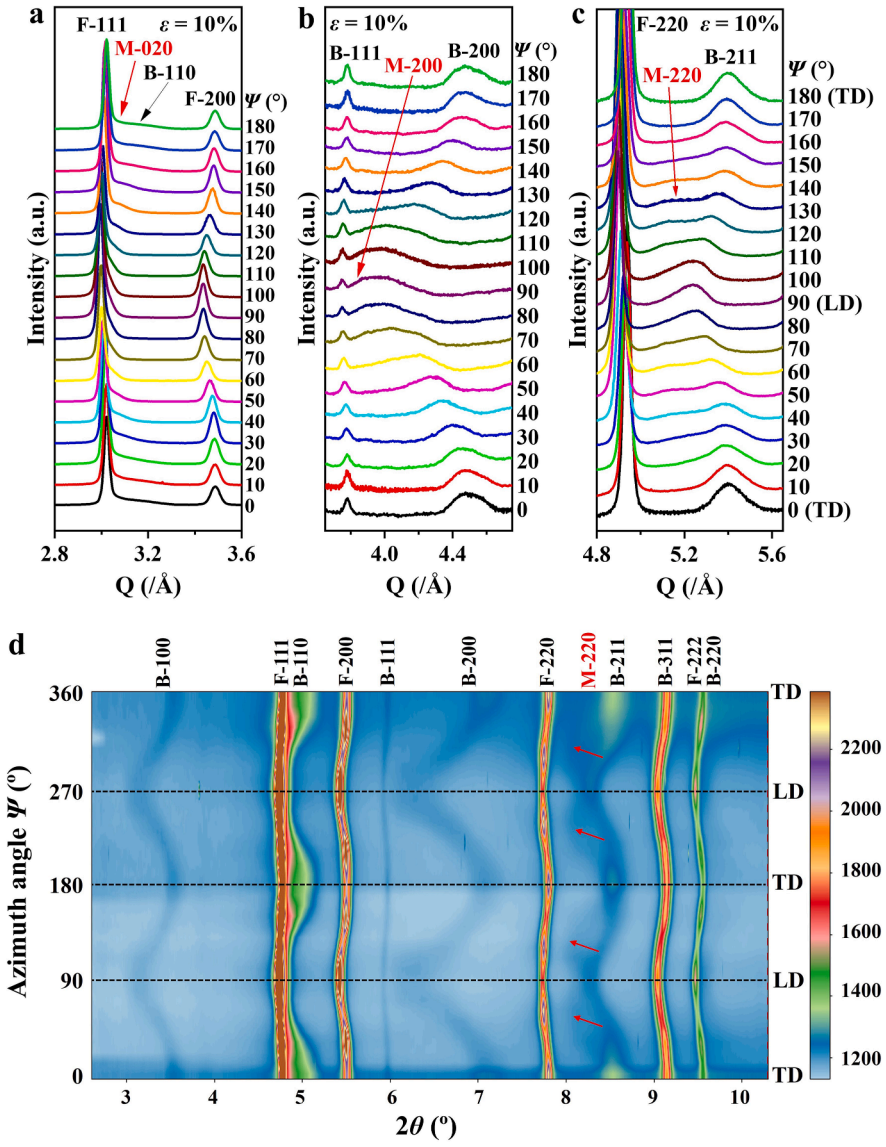

Fig. 8. 1D diffraction profiles of (a) BCC/B2–110, (b) BCC/B2–200 and (c) BCC/B2–211 by integrating the 2D diffraction patterns along the specific Ψ from 0° to 180° over a range of ±5° at ~10% strain of the as-printed $Ni_{40}Co_{20}Fe_{10}Cr_{10}Al_{18}W_2$ EHEA (M denotes the martensite). (d) 2D X-ray diffraction image along the full azimuthal angle (Ψ = 0–360°) for the as-printed $Ni_{40}Co_{20}Fe_{10}Cr_{10}Al_{18}W_2$ EHEA at tensile strain of ~10%. Note that 90° and 180° correspond to the loading direction (LD) and transverse direction (TD), respectively.

increases rapidly to 3.0×10^{-3} at 1460 MPa. Above finding suggests that a higher flow stress is required to activate same number of SFs in the as-printed sample than in the annealed sample.

3.3.4. *Martensitic transformation*

To probe the possible phase transformation upon tensile deformation, we examined the orientation-dependent structural evolution by integrating the 2D diffraction patterns along azimuth angle Ψ from 0° to 180° over a range of ±5° at a large tensile strain (right before fracture) of ~10% and ~16% for the as-printed and annealed $Ni_{40}Co_{20}Fe_{10}Cr_{10}Al_{18}W_2$ EHEAs, respectively. As shown in Fig. 8, extra Bragg peaks appear near the B-{110}, B-{200}, and B-{211} reflections at the specific Ψ. All new Bragg peaks in the diffraction profiles can be indexed as the α″ martensite phase (denoted as M) with an orthorhombic structure. Specifically, the strongest M-{020} peak appears between FCC-{111} and BCC-{110} reflections at 0° and 180° (transverse direction, TD), the strongest M-{200} peak appears next to B-{200} reflection at 90° (LD), and the strongest M-{220} peak appears near B-{211} reflection at ~50° and 130°. A similar preferred orientation selection in stress/strain-induced martensitic transformation is observed in the annealed sample (Supplementary Fig. S7), and other thermo-mechanically treated AlCoCrFeNi HEAs [50,52] as well. In general, to minimize the strain energy associated with phase transformation, the martensite phase retains a crystallographic orientation relationship with the parent BCC/B2 phase, i.e., B-(110)//M-(020), B-(1$\bar{1}$0)//M-(001) and B-(002)//M-(200) [50].

We then examined the 1D diffraction profiles of different reflections at different stress levels to determine the critical stress for martensitic transformation. As shown in Fig. 9, BCC/B2-{100}, {200}, {110}, and {211} peaks of the as-printed sample start to become asymmetric as σ_T exceeds 631 MPa. The asymmetric peaks can be deconvoluted into the parent BCC/B2 peaks and the newly formed martensite peaks. Similar phenomena have been observed in the annealed sample when σ_T reaches 651 MPa (Supplementary Fig. S8), suggesting that the martensitic transformation is initiated in both as-printed and annealed samples before macroscopic yielding. With further increase in σ_T, the asymmetric peak becomes substantially wider and eventually splits into two individual peaks.

The relative changes in the integrated intensity of BCC/B2-{110} and martensite-{020} diffraction peaks along TD can provide information about the volume fraction changes of the specific phases during deformation. As shown in Fig. 10a and c, for the as-printed sample, when σ_T is above ~650 MPa, the integrated intensity of BCC/B2-{110} peak starts to decrease slowly. Correspondingly, the integrated intensity of

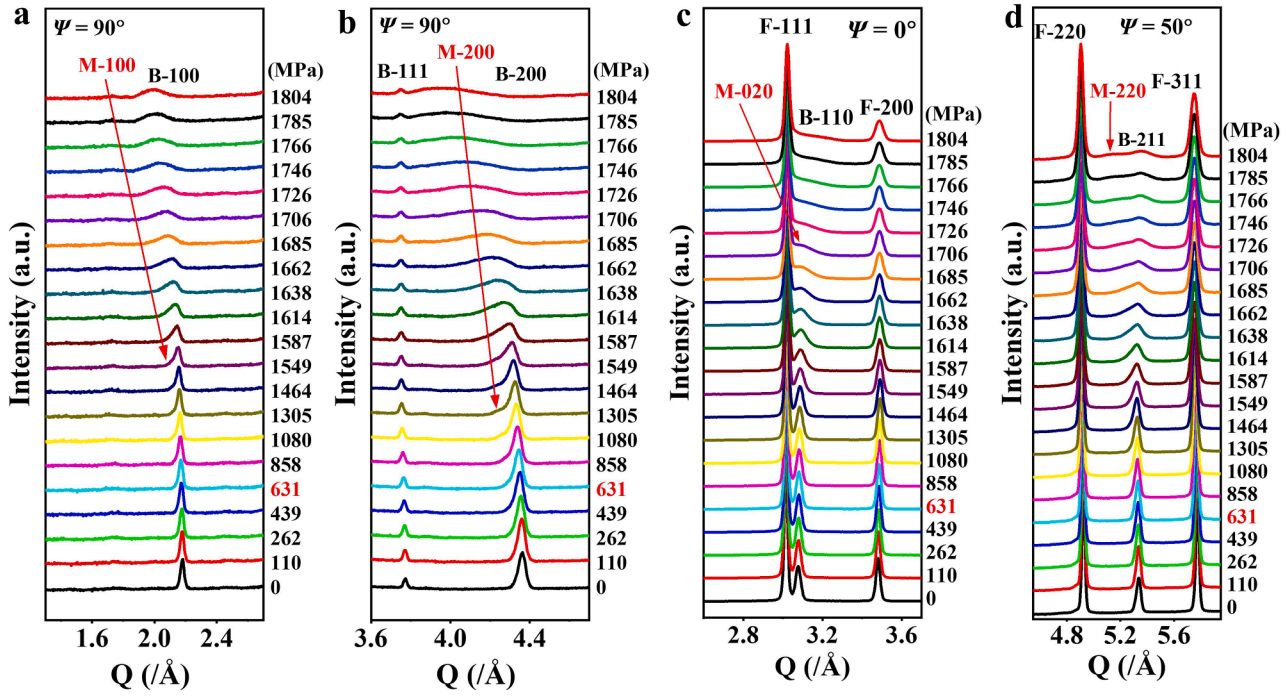

Fig. 9. HEXRD spectra of (a) B2–100 at Ψ = 90° (LD), (b) BCC/B2–200 at Ψ = 90° (LD), (c) BCC/B2–110 at Ψ = 0° (TD) and (d) BCC/B2–211 at Ψ = 50° as a function of σ_T during tensile loading of the as-printed $Ni_{40}Co_{20}Fe_{10}Cr_{10}Al_{18}W_2$ EHEA (M denotes the martensite), showing the occurrence of martensitic transformation at $\sigma_T \approx$ 631 MPa (highlighted in red). (For interpretation of the references to color in this figure legend, the reader is referred to the web version of this article).

martensite-{020} peak begins to increase slightly. Although the martensite transformation initiates before the macroscopic yielding of the bulk sample, the transformation rate of martensite stays very slow up to ~6% strain (~1600 MPa), as shown in Fig. 10a and c. Further increase in σ_T above ~1600 MPa ($\varepsilon_T >$ ~6%) results in a more rapid increase in the volume fraction of martensite. A remarkable increase in dislocation multiplication rate in the as-printed BCC/B2 lamellae at $\varepsilon_T \approx$ 6% is noteworthy (Fig. 6b). After that, the integrated intensity of martensite-{020} peak is prone to saturate as σ_T reaches 1800 MPa (ε_T >8%). In comparison, the BCC/B2-{110} peak intensity of the annealed EHEA experiences a large drop starting at $\sigma_T \approx$ 760 MPa ($\varepsilon_T \approx$ 0.5%), followed by a slower decrease until σ_T exceeds ~1300 MPa ($\varepsilon_T >$ 8%), at which a second sharp decrease occurs. Meanwhile, the behavior of the integrated intensity of martensite-{020} is inversely proportional, with a two-step increase at ~760 MPa ($\varepsilon_T \approx$ 0.5%) and ~1300 MPa ($\varepsilon_T >$ 8%), respectively (Fig. 10b and d).

3.4. Deformation structures

To understand the origin of the sustained work hardening and large ductility of the as-printed $Ni_{40}Co_{20}Fe_{10}Cr_{10}Al_{18}W_2$ EHEA, we investigated the evolution of deformation structures at different applied strains using TEM (Fig. 11). Before deformation, a high density of dislocations is observed in FCC/$L1_2$ nanolamellae (Fig. 11 a1 and a2), while few dislocations are seen in the BCC/B2 nanolamellae. These pre-existing dislocations originate from thermal residual stresses due to rapid heating and cooling cycles during L-PBF [54]. At a strain of ~2% (Fig. 11 b1), curved dislocations are comparably observed in both FCC/$L1_2$ and BCC/B2 nanolamellae, indicating the mixed characters of dislocations. In contrast to the typical straight screw dislocations in bulk BCC metals, the multiplicity of dislocation pathways in the multicomponent BCC/B2 nanolamellae contributes to the enhanced work hardening and ductility [62]. Note that few SFs start to be observed in some FCC/$L1_2$ nanolamellae (Fig. 11 b2). As the strain increases to ~5% (Fig. 11 c1 and c2), SFs become more dominant in FCC/$L1_2$ nanolamellae. A few curved dislocations could still be observed. In the BCC/B2 nanolamellae, dislocation density appears much higher in regions near the tip of SFs in FCC/$L1_2$ nanolamellae (Fig. 11 c2), suggesting that dislocations in BCC/B2 nanolamellae tend to nucleate and multiplicate more rapidly in the vicinity of SFs at the lamellar interfaces. At a strain of ~17%, a large increase in SF density in FCC/$L1_2$ nanolamellae occurs while ordinary, curved dislocations are barely visible, indicating SF-mediated deformation behavior. In BCC/B2 nanolamellae, the increase in dislocation density is clearly noticeable. This high density of dislocations in BCC/B2 nanolamellae reasonably interprets the substantial work hardening capability of the BCC/B2 phase, as also revealed by *in-situ* synchrotron HEXRD (Fig. 5d). Additionally, a large number of defects including dislocations and SFs are found at the phase interfaces using HRTEM (Fig. 12), suggesting the important role of semi-coherent interfaces that can serve as effective dislocation barriers and sinks [63].

The deformation structures in the annealed $Ni_{40}Co_{20}Fe_{10}Cr_{10}Al_{18}W_2$ EHEA after ~23% strain (corresponding to the ultimate tensile strength) were also investigated to understand the exceptional work hardening capability of the annealed sample. Compared to the as-printed sample, a much higher density of defects is observed that aggregate at the lamellar interfaces, as evidenced by the strong dark contrast (Fig. 13a). This suggests two possible mechanisms: first, the high-temperature annealing may have changed the local chemical composition, residual stresses, or structural ordering at or near the lamellar interfaces, which could improve dislocation multiplication; second, ordinary dislocation slip could still be largely active at large strains in the annealed FCC nanolamellae unlike in the as-printed sample, and dislocations could more easily cross-slip and move along the interfaces. In addition, a similar amount of SF ribbons is observed in the annealed FCC nanolamellae (ε = 23%) as that in the as-printed FCC/$L1_2$ nanolamllae (ε = 17%) (Fig. 11 d1-d2 and Fig. 13b-c), although the annealed sample undergoes a much lower flow stress. The above finding reflects that SFs can be activated more easily in the annealed FCC nanolamellae at a lower flow stress and the origins will be discussed later. Moreover, compared to the as-printed BCC/B2 nanolamellae, a higher density of dislocations is discerned in the annealed BCC/B2 nanolamellae (Fig. 13a), suggesting the superior dislocation storage capability of the annealed BCC/B2 nanolamellae.

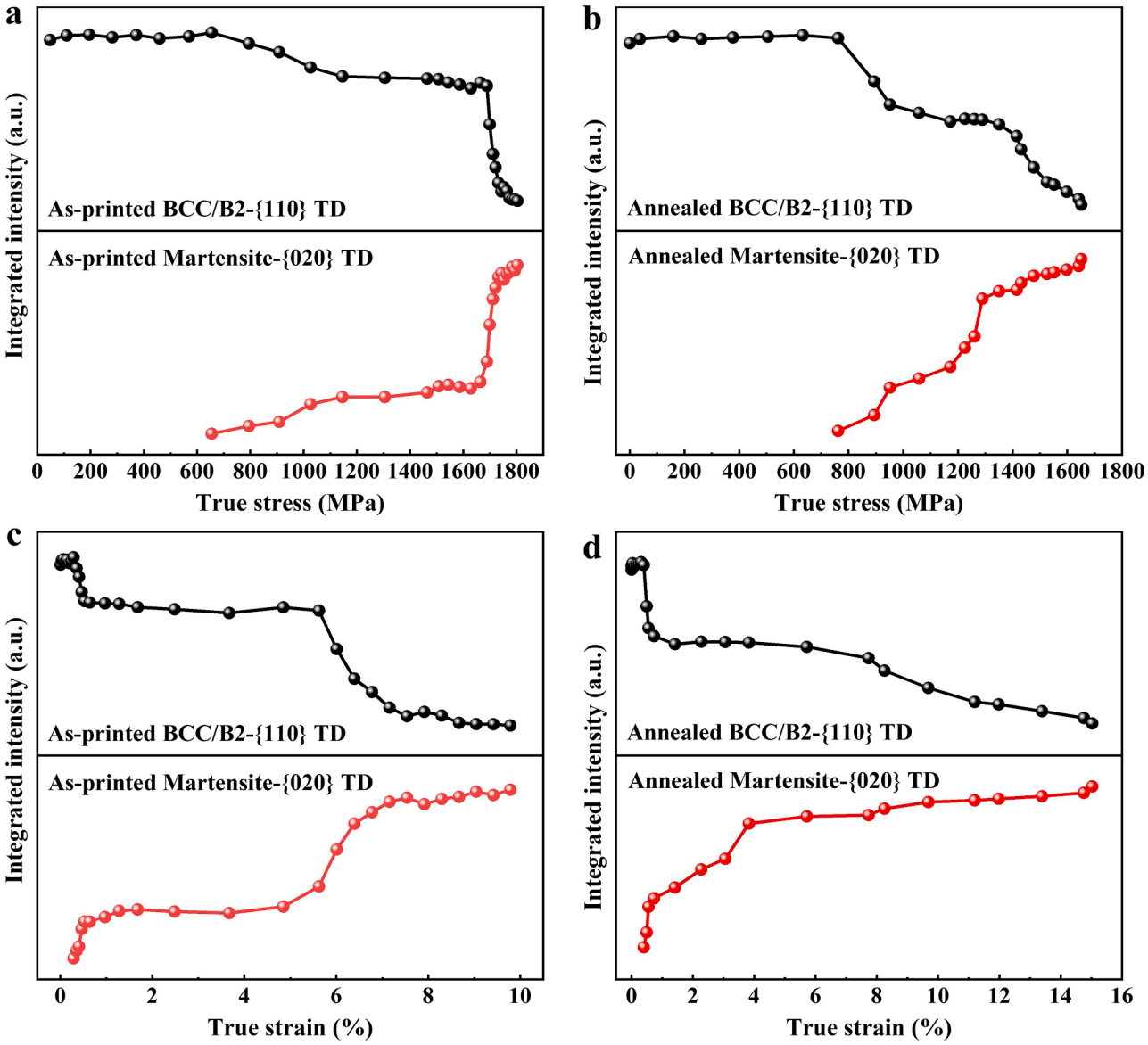

Fig. 10. Evolution of martensite during deformation measured by HEXRD along TD. (a, b) Integrated intensity of BCC/B2-{110} and Martensite-{020} diffraction peaks along TD, plotted as a function of true stress for the as-printed and annealed $Ni_{40}Co_{20}Fe_{10}Cr_{10}Al_{18}W_2$ EHEAs, respectively. (c, d) Same as (a, b) except for plotted as a function of true strain.

4. Discussions

4.1. Origin of ultrahigh yield strength

The yield strength of polycrystalline metal alloys is determined by characteristic microstructural features such as solute atoms, boundaries/interfaces, dislocations, and precipitates [64]. Grain refinement is one of the most common strategies used to strengthen a material. Reducing the average grain size gives rise to a larger volume fraction of grain boundaries, which act as strong pinning points to impede the dislocation movement and hence increase the yield strength following the well-known Hall-Petch relationship [65,66]:

$$\sigma_{YS} = \sigma_0 + kd^{-1/2} \tag{7}$$

where σ_0 is the intrinsic lattice friction stress, d the average grain size, k the strengthening coefficient associated with the strength of grain boundaries. An increase in lattice friction leads to a higher yield strength by increasing the stress necessary to move dislocations within the grain matrix. Our $Ni_{40}Co_{20}Fe_{10}Cr_{10}Al_{18}W_2$ EHEA contains multi-principal elements, which is the pillar of the HEA concept. In general, the severe crystal lattice distortion in HEAs contributes to the lattice friction stress by ~100–200 MPa [67–69].

During L-PBF, the high cooling rates help suppress grain growth, which we adopt here as a strategy to achieve highly refined lamellae at the nanoscale compared to conventional counterparts. In dual-phase lamellar structures, yielding is expected to occur when the critical stress for dislocation transmission through the lamellar interfaces is reached [70,71]. Recall that the yield strength of our L-PBF $Ni_{40}Co_{20}Fe_{10}Cr_{10}Al_{18}W_2$ EHEA is twofold higher than that of the as-cast counterpart. In fact, the average interlamellar spacing of our as-printed sample is ~5 times smaller than that of the as-cast counterpart, which approximately doubles the $kd^{-1/2}$ term in Eq. (7). This comparison underscores the dominant role of nanolamellar interfaces in strengthening the additively manufactured $Ni_{40}Co_{20}Fe_{10}Cr_{10}Al_{18}W_2$ EHEA.

The high density of printing-induced dislocations in FCC/$L1_2$ nanolamellae also makes a contribution to the high yield strength of the as-

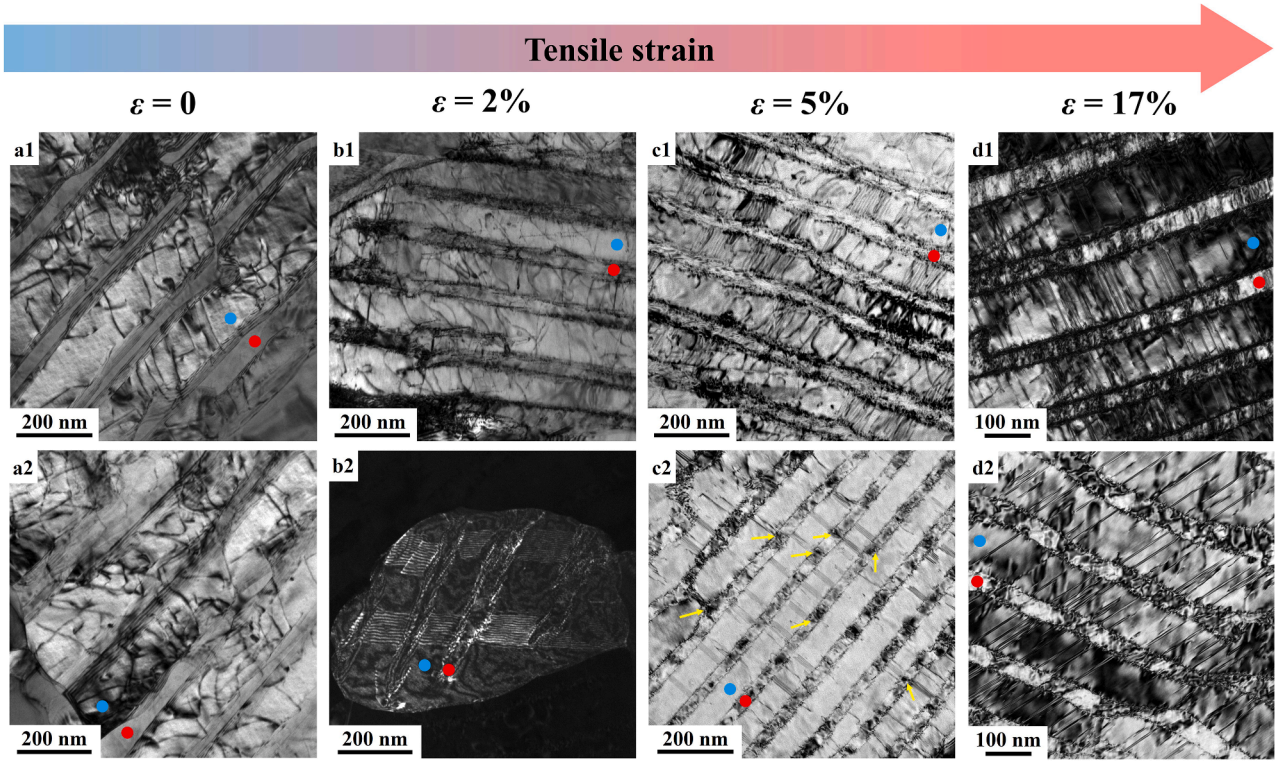

Fig. 11. TEM images of deformation structures in the as-printed $Ni_{40}Co_{20}Fe_{10}Cr_{10}Al_{18}W_2$ EHEA at different tensile strains. BCC/B2 nanolamella is indicated by the red dot and FCC/$L1_2$ nanolamella is indicated by the blue dot. The yellow arrows indicate that dislocations in BCC/B2 nanolamellae tend to nucleate and multiplicate more rapidly in the regions near the tip of SFs at the lamellar interfaces (For interpretation of the references to color in this figure legend, the reader is referred to the web version of this article).

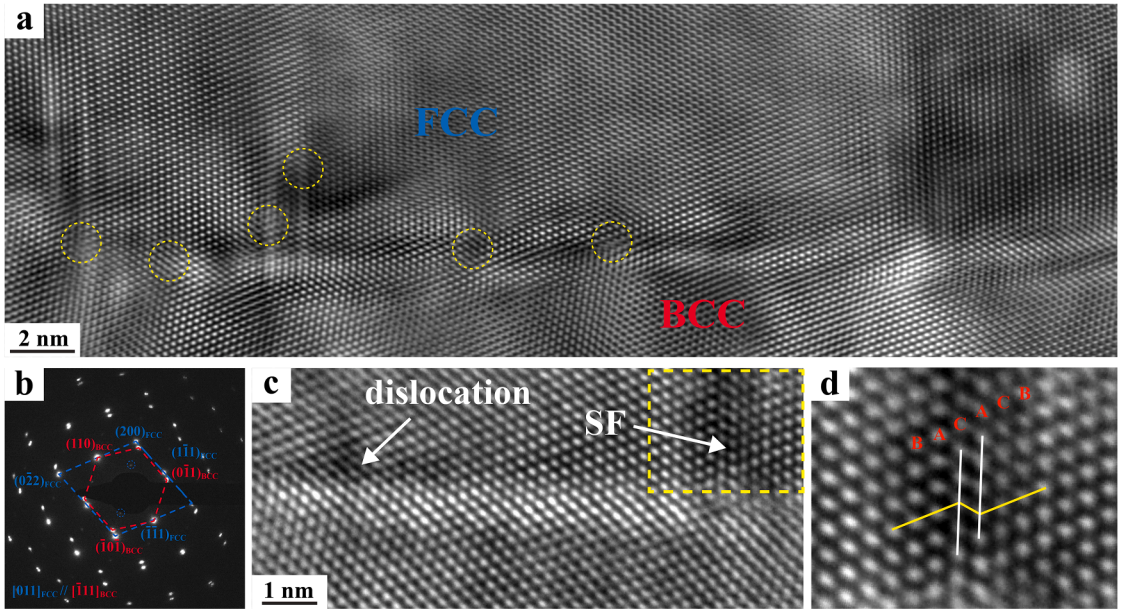

Fig. 12. Crystal lattice defects at phase interface in the as-printed $Ni_{40}Co_{20}Fe_{10}Cr_{10}Al_{18}W_2$ EHEA deformed to 17% strain. (a) HRTEM micrograph showing a high density of defects (yellow circles show some examples) at the lamellar interface. (b) Corresponding SAED pattern indicating the K-S orientation relationship between the two phases. (c) Enlarged HRTEM micrograph showing a dislocation and a SF at the interface. (d) Higher magnification HRTEM micrograph of the yellow boxed region in (c) showing a SF marked by the BCACAB-stacking sequence (For interpretation of the references to color in this figure legend, the reader is referred to the web version of this article).

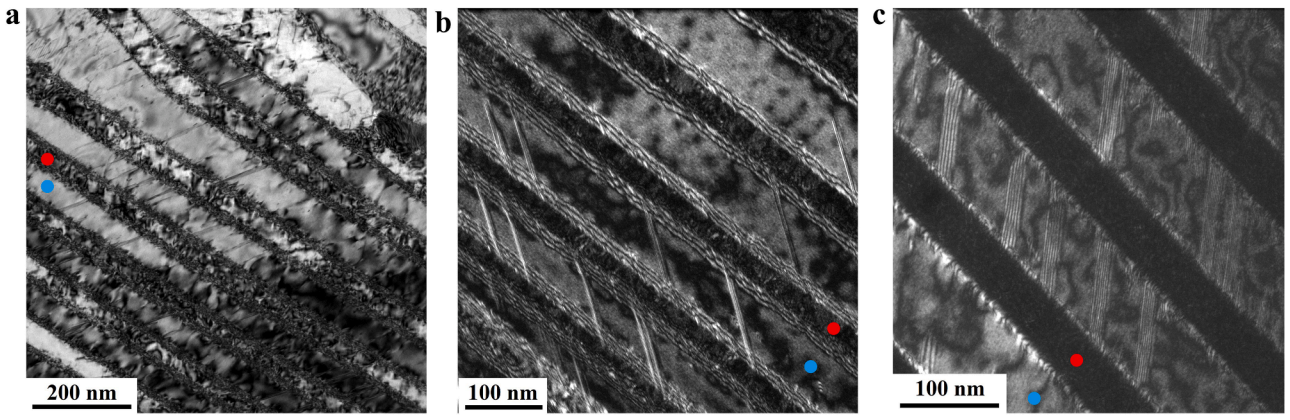

Fig. 13. Deformation structures in the annealed $Ni_{40}Co_{20}Fe_{10}Cr_{10}Al_{18}W_2$ EHEA after ~23% deformation. BCC/B2 nanolamella is indicated by the red dot and FCC nanolamella is indicated by the blue dot. (a) BF TEM image showing high density of dislocations in BCC/B2 nanolamellae and phase interface. (b-c) Dark-field (DF) TEM images highlighting numerous SFs extended through FCC nanolamellae (For interpretation of the references to color in this figure legend, the reader is referred to the web version of this article).

Table A1
First-principles DFT calculation results.

Sample condition	Composition/at.%	Lattice constant/Å	E_{usf}/mJ/m^2		E_{isf}/mJ/m^2	
			Ferromagnetic	Paramagnetic	Ferromagnetic	Paramagnetic
As-printed FCC/$L1_2$	$Al_{11}Co_{22}Cr_{12}Fe_{12}Ni_{40}W_3$	3.6037	131.25	117.55	65.23	57.44
Annealed FCC	$Al_9Co_{26}Cr_{15}Fe_{14}Ni_{34}W_2$	3.5883	81.22	76.89	42.97	37.16

printed sample [21,35]. We estimate this strengthening effect using the Taylor hardening law [72]:

$$\Delta\sigma_d = M\alpha Gb\rho^{1/2} \tag{8}$$

where M is the Taylor factor (3.06 for the FCC/$L1_2$ phase, measured from EBSD), α is the dimensionless pre-factor (about 0.2 for the FCC/$L1_2$ phase [64]), G is the shear modulus (78 GPa for the FCC/$L1_2$ phase, derived from HEXRD measurements), b is the magnitude of Burgers vector (0.255 nm for the FCC/$L1_2$ phase, measured by HEXRD) and ρ is the pre-existing dislocation density (1.2×10^{14} m^{-2} for the FCC/$L1_2$ phase). Considering the volume fraction of FCC/$L1_2$ phase is as high as 72%, the pre-existing dislocations from L-PBF contribute to an increase of yield strength $\Delta\sigma_d = 96$ MPa.

Recall that the yield strength of the as-printed FCC/$L1_2$ phase is ~500 MPa higher than that of the annealed FCC phase (Fig. 5c), which suggests that $L1_2$ structural ordering also plays an important role in elevating the yield strength of the as-printed sample (Supplementary Fig. S4). In dual-phase lamellar structures, yielding occurs first in the weaker FCC/$L1_2$ lamellae. $L1_2$ is an ordered FCC structure that can effectively increase the yield strength by restricting the number of available slip systems. The sparsely-distributed BCC nano-precipitates inside the relatively coarser BCC/B2 nanolamellae (Fig. 1h) could also hinder the dislocation motion to strengthen the material. However, different from the uniformly dispersed BCC nano-precipitates in B2 lamellae of other thermo-mechanically treated EHEAs (e.g., AlCoCrFeNi$_{2.1}$) where BCC nano-precipitates can effectively enhance the yield strength through dispersion strengthening [44], the strengthening effect from the sparsely-distributed BCC nano-precipitates inside the relatively coarser BCC/B2 nanolamellae only in our as-printed sample is expected to be negligible.

In summary, the high yield strength of the additively manufactured $Ni_{40}Co_{20}Fe_{10}Cr_{10}Al_{18}W_2$ EHEA is mainly governed by the refined nanolamellar structure enabled by rapid solidification of L-PBF, and further enhanced by the pre-existing dislocations and ordered $L1_2$ structures. These unique microstructural features not only collectively result in significant resistance to dislocation motion for elevating the yield strength, but also promoting the work hardening capability, as discussed below.

4.2. Evolution of deformation mechanisms

4.2.1. Deformation mechanisms in FCC/$L1_2$ nanolamellae

We first discuss the deformation mechanisms in FCC/$L1_2$ nanolamellae. In general, a material's deformation mechanisms depend on the applied flow stress and the critical stresses required for the activation of different deformation carries (such as dislocations, SFs, twins, etc.). TEM observations suggest that the deformation of the as-printed FCC/$L1_2$ nanolamellae is mediated by dislocation slip and SFs (Fig. 11). Based on classical dislocation theory, the critical shear stress required to nucleate a full dislocation 1/2<110> (τ_F) or the Shockley partial dislocations 1/6<112> (τ_P) to generate SFs and deformation twins can be estimated using the following equations [73]

$$\tau_F(d) = \frac{2\alpha\mu b_F}{d} \tag{9}$$

$$\tau_P(\gamma, d) = \frac{2\alpha\mu b_P}{d} + \frac{\gamma}{b_P} \tag{10}$$

where γ is the SFE; α a parameter reflecting the character of dislocations; μ the shear modulus; and b_F and b_P the magnitudes of Burgers vectors of full and partial dislocations, respectively. As suggested by Eqs. (9) and (10), the preference for dislocations, SFs, and deformation twins is strongly dependent on SFE (γ) and the characteristic dislocation source size (d) [74]. First, SFE determines the ease of dissociation of a perfect dislocation into two partials and the propensity for the formation of SFs [61]. As reported in austenitic steels, the deformation mechanisms often change from dislocation slip (≥45 mJ/m^2) to twinning (20–45 mJ/m^2) with the decrease of SFE [75]. Besides SFE, the characteristic dislocation source size (d), (in our case, d denotes the FCC/$L1_2$ lamellar thickness λ_{FCC}) also plays an important role in affecting the deformation schemes. As λ_{FCC} decreases, the partial dislocations would increasingly prevail over full dislocations [76].

We first discuss the SF behavior in the as-printed FCC/$L1_2$ nanolamellae. The first-principles DFT calculation result suggests that the intrinsic SFE of the as-printed FCC/$L1_2$ nanolamellae is as high as 57 mJ/m^2 (see Appendix), which is not sufficient to activate partial dislocations and SFs. Therefore, sufficient dislocation activities may precede the formation of SFs. Although SFs initiate in some FCC/$L1_2$ nanolamellae that bear higher stresses at 2% strain (Fig. 11 b2), TEM observations confirm that the early-stage plastic deformation of FCC/$L1_2$ nanolamellae is mostly operated by full dislocation slip (Fig. 11 a1 and b1). As deformation proceeds after ~5% strain, SFs become prevalent (Fig. 11 c1-d2) as the critical stress required to nucleate Shockley partial dislocations 1/6<112> to generate SFs is reached for the majority of FCC/$L1_2$ nanolamellae with different orientations. However, SFs are not readily achievable in conventional dual-phase microlamellar EHEAs with similar compositions such as $AlCoCrFeNi_{2.1}$ [16], and $Al_{19}Fe_{20}Co_{20}Ni_{41}$ [53]. The above findings highlight the advantages of harnessing the extreme processing conditions of L-PBF for microstructural refinement at the nanoscale to promote SF formation.

HEXRD and TEM characterizations indicate that SFs can be more easily activated in the annealed sample compared to the as-printed sample (Figs. 7b, 11, and 13), which is likely related to the change of SFE and thickness of FCC/$L1_2$ nanolamellae after heat treatment. First, SFE mainly changes with the chemical composition of a material. In our work, starting from the far-from-equilibrium microstructure in the as-printed state, the high-temperature heat treatment promotes atomic diffusion and element partitioning between the alternating dual-phase nanolamellae. As shown in Table 1, the annealed FCC nanolamellae are further depleted in Al and Ni which are characteristic of high SFE. Thus, the annealed FCC nanolamellae are expected to have a lower SFE compared to those in the as-printed sample. Our first-principles DFT calculation results verify that the intrinsic SFE of FCC/$L1_2$ nanolamellae is reduced from 57 mJ/m^2 to 37 mJ/m^2 after heat treatment (see Appendix). Second, after heat treatment, the average thickness of FCC/$L1_2$ nanolamellae decreases from 119 nm to 95 nm as a result of interface migration at the elevated temperature. The simultaneously reduced SFE and λ_{FCC} after heat treatment explain the abundant SFs observed in the annealed FCC nanolamellae at a lower flow stress (Fig. 13).

4.2.2. Deformation mechanisms in BCC/B2 nanolamellae

Second, we discuss the deformation mechanisms in BCC/B2 nanolamellae. Considering the strain compatibility required between the co-deforming FCC/$L1_2$ and BCC/B2 phases, the deformation behavior of BCC/B2 nanolamellae would be strongly influenced by the neighboring FCC/$L1_2$ nanolamellae and lamellar interfaces. Dislocation multiplication in the as-printed BCC/B2 nanolamellae remains very slow during the initial 2% strain. Simultaneously, when SFs dominate above 5% strain in the as-printed FCC/$L1_2$ nanolamellae, more extensive dislocation multiplication is observed in BCC/B2 nanolamellae, especially near the tip of SFs in the neighboring FCC/$L1_2$ nanolamellae (Fig. 11 c2). Meanwhile, a thick contrast appears at the lamellar interfaces, suggesting the extraordinary dislocation activities likely resulting from the full dislocation cross-slip and movement along the interfaces, and the pile-up of SFs at the interfaces. The extended SFs in FCC/$L1_2$ nanolamellae and the numerous defects aggregated at lamellar interfaces can effectively enhance local stresses to promote nucleation/multiplication of dislocations and martensitic transformation in the neighboring BCC/B2 nanolamellae. This can be further confirmed by the rapid increase in ρ_{BCC} (Fig. 6b) and martensitic phase fraction (Fig. 10c) at ~6% strain.

Besides extensive dislocation multiplication in BCC/B2 nanolamellae, HEXRD analysis also suggests the occurrence of SIMT (Fig. 9). SIMT can significantly increase the lattice distortion to further strengthen the material, as evidenced by the abnormally large lattice strain of B-{200} plane family along LD (Fig. 5a-b). Similar phenomenon has been found by others in previous studies as well [50,52]. In addition, the simultaneous increase in the volume fraction of martensite and ρ_{BCC} at $\varepsilon_T \approx 6\%$ elucidates that SIMT is conducive to enhancing the dislocation multiplication rate, thus contributing to the sustained work hardening of BCC/B2 phase (Figs. 5d, 6b and 10c). In other thermo-mechanically treated duplex HEAs, SIMT has also proven to be an effective mechanism for promoting dislocation multiplication to enhance the deformability and working hardening of the multi-component B2 phase [52,77].

With regard to SIMT, thermodynamically, applied stress provides a mechanical driving force which adds to the chemical free energy change due to transformation and determines the onset of the transformation [78]. Besides applied stress, martensitic transformation is also strongly affected by the spatial confinement imposed by precipitates. The small precipitates size and narrow inter-precipitates spacing have been reported to heavily hinder the martensitic transformation [79]. Compared to the annealed sample, the higher SFE in the as-printed FCC/$L1_2$ nanolamellae and the sparsely-distributed nano-precipitates in the relatively coarser BCC/B2 nanolamellae operate collectively to retard the martensitic transformation in the as-printed BCC/B2 nanolamellae, as evidenced by the nearly constant volume fraction of martensite as ε_T evolves from ~2% to ~5% (Fig. 10c). Further increase of the martensite volume fraction requires higher applied stresses to overcome the heightened energy barrier for transformation. Although the martensite volume fraction and ρ_{BCC} rapidly increase when σ_T exceeds ~1600 MPa (ε_T > ~6%), they saturate soon as ε_T increases to 8%. These results suggest that the defect storage capability of BCC/B2 nanolamellae is already exhausted. In contrast, the annealed BCC/B2 nanolamellae are free of precipitates and contain a lower density of dislocations. Additionally, the annealed FCC nanolamellae have a smaller SFE which triggers SFs more easily at a lower stress. Although the annealed sample displays a lower yield strength, the dissolution of BCC nano-precipitates in BCC/B2 nanolamellae helps to release the spatial confinement and contributes to the sustainable increase of the martensite volume fraction and dislocation density, and eventually results in the higher work hardening rates (Figs. 4b and 5c-d).

In conclusion, the SF-mediated plasticity in FCC/$L1_2$ nanolamellae and the accumulation of vast defects at lamellar interfaces after ~5% strain can effectively elevate local stresses to enhance dislocation multiplication and martensitic transformation in BCC/B2 nanolamellae. The cooperative deformation of FCC/$L1_2$ and BCC/B2 nanolamellae, assisted by the semi-coherent lamellae interfaces, is beneficial for the sustained work hardening and large ductility of the additively manufactured $Ni_{40}Co_{20}Fe_{10}Cr_{10}Al_{18}W_2$ EHEA.

5. Conclusions

In this study, we use L-PBF to improve mechanical properties of a dual-phase $Ni_{40}Co_{20}Fe_{10}Cr_{10}Al_{18}W_2$ EHEA by refining the lamellar thickness to nanoscale. An ultrahigh yield strength of ~1.4 GPa is achieved with a large tensile ductility of ~17%. This doubles the yield strength of the as-cast counterpart without a considerable sacrifice in ductility. We used *in-situ* synchrotron HEXRD and advanced electron microscopy to uncover the microstructures and deformation mechanisms underlying the significantly enhanced mechanical properties in the additively manufactured $Ni_{40}Co_{20}Fe_{10}Cr_{10}Al_{18}W_2$ EHEA. Key observations are summarized below:

(1) The strong thermal gradients and high cooling rates inherent to L-PBF provide a unique pathway to achieve non-equilibrium, highly-refined nanolamellar structures in a dual-phase $Ni_{40}Co_{20}Fe_{10}Cr_{10}Al_{18}W_2$ EHEA.
(2) The high strength of the as-printed $Ni_{40}Co_{20}Fe_{10}Cr_{10}Al_{18}W_2$ EHEA primarily results from the refined nanolamellar structures and is further enhanced by the pre-existing dislocations from rapid solidification of L-PBF and ordered $L1_2$ structures.
(3) The large ductility originates from the sequentially activated multiple deformation mechanisms in FCC/$L1_2$ and BCC/B2 nanolamellae. The deformation mechanism of FCC/$L1_2$

nanolamellae evolves from full dislocation slip to SF nucleation at around 5% strain. Simultaneously, the semi-coherent lamellar interfaces serve as the preferred sites for defect aggregation which effectively elevates local stresses that enhance dislocation multiplication and martensitic transformation in the neighboring BCC/B2 nanolamellae.

(4) Post-printing heat treatment allows us to further tune the non-equilibrium microstructures and deformation mechanisms. Stronger elemental partitioning between dual phases can significantly reduce SFE to facilitate the formation of SFs in FCC nanolamellae. The dissolution of BCC nano-precipitates in BCC/B2 nanolamellae can relieve the spatial confinement which further promotes martensitic transformation and enhances the work hardening capability.

Declaration of Competing Interest

The authors declare that they have no known competing financial interests or personal relationships that could have appeared to influence the work reported in this paper.

Acknowledgments

Wen Chen at UMass Amherst acknowledges support from the US National Science Foundation (DMR-2004429 and DMR-2238204) and UMass Amherst Faculty Startup Fund. M.W., J.B. F., and T.V.'s work at Lawrence Livermore National Laboratory (LLNL) was performed under the auspices of the U.S. Department of Energy (DOE) under Contract No. DE-AC52–07NA27344. M.W. and T.V. would like to thank Tony Li at LLNL for helping with PED crystal orientation mapping. Wei Chen at Illinois Institute of Technology acknowledges support from the US National Science Foundation (DMR-1945380). *In-situ* high-energy X-ray diffraction work was carried out at the Advanced Photon Source (Beamline 11-ID-C and 1-ID-E), which is a US DOE user facility at Argonne National Laboratory. Authors would like to thank Jun-Sang Park at beamline 1-ID-E and Kevin A. Beyer at beamline 11-ID-C for the support. Some work is based on research conducted at the Center for High-Energy X-ray Sciences (CHEXS) at CHESS, which is supported by the National Science Foundation (BIO, ENG and MPS Directorates) under award DMR-1829070. Dr. Amlan Das' experimental support at CHEXS is acknowledged. This research also used Spallation Neutron Source (SNS), which is a US DOE user facility at the Oak Ridge National Laboratory (ORNL), sponsored by the Scientific User Facilities Division, Office of Basic Energy Sciences.

Supplementary materials

Supplementary material associated with this article can be found, in the online version, at doi:10.1016/j.actamat.2023.119179.

Appendix. First-principles density functional theory calculations

First-principles calculations on SFE of AlCoCrFeNiW HEAs were performed with the EMTO—CPA package in this work. The exact muffin-tin orbital (EMTO) [80] method uses optimized overlapping muffin-tin potential spheres to represent the exact one-electron potential [81]. The one-electron equations were solved with the scalar relativistic approximation and the soft-core method. The coherent-potential approximation (CPA) [82] method simulates the chemical disorder which is an important feature for HEAs. The Perdew-Burke-Ernzerhof generalized gradient approximation (PBE) [83] was used to approximate the exchange-correlation functional, and the full charge density (FCD) method improved the accuracy of total energy calculation. The EMTO Green's function was calculated self-consistently for 16 complex energy points that distributed exponentially [84]. Since the magnetic state [85] influences the SFE in HEAs, the ferromagnetic and paramagnetic states described by the disordered local magnetic moment (DLM) [86] were chosen as two initial magnetic conditions.

The static equation of states (EOS) was determined from energies of twelve different atomic volumes. The equilibrium lattice constant was obtained by fitting the Birch–Murnaghan EOS [87]. The SFE was calculated as the excess total energy associated with the formation of a SF in an ideal FCC lattice. To eliminate the interactions between a SF with its periodic images, a supercell model of 9 FCC (111) layers [88] was used. The SF is created by sliding the z-axis perpendicular to the successive (111) planes with a series of displacement $n\mathbf{b}_p$ ($\mathbf{b}_p = a_0<\bar{2}11>/6$ is Burgers vector, a_0 is the lattice constant) in the superlattice, while the lattice with $0.5\mathbf{b}_p$ displacement represents unstable SF as the energy barrier during the SF formation. The k-point mesh was carefully tested for convergence, and the $12 \times 24 \times 3$ mesh was used in all calculations to achieve an accuracy of 10^{-6} Ry/site. For each sliding step, the interlayer distances corresponding to the slip layer were optimized [89], while the other interlayer distances were fixed at the equilibrium state.

Based on the STEM-EDX results on different FCC lamellae of the as-printed and annealed EHEAs, different compositions were selected for the DFT calculations. Determined from the Birch–Murnaghan EOS, the average lattice constant of the as-printed sample is 3.6037 Å which is very close to the experimental observation of 3.5908 Å with a 0.36% difference. The better agreement is achieved in the annealed sample for which the calculated lattice constant is 3.5883 Å and the experimental lattice constant is 3.5874 Å.

As shown in Table A1, the SFEs of the annealed samples are lower than the as-printed samples, suggesting more SFs can be formed in annealed samples rather than in as-printed samples. Especially in the paramagnetic state, the intrinsic SFE E_{isf} is lower than 40 mJ/m^2 which is a common criterion [90] for predicting twinning deformation. The difference in unstable SFEs E_{usf} between the as-printed and annealed samples is even more pronounced at about 40%. The lower E_{usf} indicates a low energy barrier for the SF formation, which can lead to a significant difference in the stacking fault density. During the application of external stress, however, a higher energy barrier for the SF formation can still be overcome by completing the partial dislocation slip, which can be an explanation for the large increase in the stacking fault density in the as-printed sample above ~5% strain.

References

[1] Y. Wang, M. Chen, F. Zhou, E. Ma, High tensile ductility in a nanostructured metal, Nature 419 (2002) 912–915.
[2] M.A. Meyers, A. Mishra, D.J. Benson, Mechanical properties of nanocrystalline materials, Prog. Mater. Sci. 51 (2006) 427–556.
[3] Y. Li, D. Raabe, M. Herbig, P.P. Choi, S. Goto, A. Kostka, H. Yarita, C. Borchers, R. Kirchheim, Segregation stabilizes nanocrystalline bulk steel with near theoretical strength, Phys. Rev. Lett. 113 (2014), 106104.
[4] Z.C. Cordero, B.E. Knight, C.A. Schuh, Six decades of the Hall–Petch effect – a survey of grain-size strengthening studies on pure metals, Int. Mater. Rev. 61 (2016) 495–512.

[5] Y.M. Wang, E. Ma, Three strategies to achieve uniform tensile deformation in a nanostructured metal, Acta Mater. 52 (2004) 1699–1709.
[6] R.O. Ritchie, The conflicts between strength and toughness, Nat. Mater. 10 (2011) 817–822.
[7] E. Ma, T. Zhu, Towards strength–ductility synergy through the design of heterogeneous nanostructures in metals, Mater. Today 20 (2017) 323–331.
[8] E. Ma, X. Wu, Tailoring heterogeneities in high-entropy alloys to promote strength–ductility synergy, Nat. Commun. 10 (2019) 5623.
[9] P. Sathiyamoorthi, H.S. Kim, High-entropy alloys with heterogeneous microstructure: processing and mechanical properties, Prog. Mater. Sci. 123 (2022), 100709.
[10] J. Li, Q. Zhang, R. Huang, X. Li, H. Gao, Towards understanding the structure–property relationships of heterogeneous-structured materials, Scr. Mater. 186 (2020) 304–311.
[11] L. Lu, Y. Shen, X. Chen, L. Qian, K. Lu, Ultrahigh Strength and High Electrical Conductivity in Copper, Science 304 (2004) 422–426.
[12] Y. Wang, J. Li, A.V. Hamza, T.W. Barbee, Ductile crystalline–amorphous nanolaminates, Proc. Natl. Acad. Sci 104 (2007) 11155–11160.
[13] Z. Cheng, H. Zhou, Q. Lu, H. Gao, L. Lu, Extra strengthening and work hardening in gradient nanotwinned metals, Science 362 (2018) eaau1925.
[14] W.L. Li, N.R. Tao, K. Lu, Fabrication of a gradient nano-micro-structured surface layer on bulk copper by means of a surface mechanical grinding treatment, Scr. Mater. 59 (2008) 546–549.
[15] T.H. Fang, W.L. Li, N.R. Tao, K. Lu, Revealing extraordinary intrinsic tensile plasticity in gradient nano-grained copper, Science 331 (2011) 1587–1590.
[16] P. Shi, W. Ren, T. Zheng, Z. Ren, X. Hou, J. Peng, P. Hu, Y. Gao, Y. Zhong, P. K. Liaw, Enhanced strength–ductility synergy in ultrafine-grained eutectic high-entropy alloys by inheriting microstructural lamellae, Nat. Commun. 10 (2019) 489.
[17] T. Yang, Y.L. Zhao, Y. Tong, Z.B. Jiao, J. Wei, J.X. Cai, X.D. Han, D. Chen, A. Hu, J. J. Kai, Multicomponent intermetallic nanoparticles and superb mechanical behaviors of complex alloys, Science 362 (2018) 933–937.
[18] D. Herzog, V. Seyda, E. Wycisk, C. Emmelmann, Additive manufacturing of metals, Acta Mater. 117 (2016) 371–392.
[19] S. Gorsse, C. Hutchinson, M. Gouné, R. Banerjee, Additive manufacturing of metals: a brief review of the characteristic microstructures and properties of steels, Ti-6Al-4V and high-entropy alloys, Sci. Technol. Adv. Mater. 18 (2017) 584–610.
[20] T. DebRoy, H.L. Wei, J.S. Zuback, T. Mukherjee, J.W. Elmer, J.O. Milewski, A. M. Beese, A. Wilson-Heid, A. De, W. Zhang, Additive manufacturing of metallic components – Process, structure and properties, Prog. Mater. Sci. 92 (2018) 112–224.
[21] Y.M. Wang, T. Voisin, J.T. McKeown, J. Ye, N.P. Calta, Z. Li, Z. Zeng, Y. Zhang, W. Chen, T.T. Roehling, Additively manufactured hierarchical stainless steels with high strength and ductility, Nat. Mater. 17 (2018) 63–71.
[22] J. Suryawanshi, K.G. Prashanth, S. Scudino, J. Eckert, O. Prakash, U. Ramamurty, Simultaneous enhancements of strength and toughness in an Al-12Si alloy synthesized using selective laser melting, Acta Mater. 115 (2016) 285–294.
[23] J.H. Martin, B.D. Yahata, J.M. Hundley, J.A. Mayer, T.A. Schaedler, T.M. Pollock, 3D printing of high-strength aluminium alloys, Nature 549 (2017) 365–369.
[24] T. Mukherjee, J.S. Zuback, A. De, T. DebRoy, Printability of alloys for additive manufacturing, Sci. Rep. 6 (2016) 19717.
[25] J. Fu, H. Li, X. Song, M.W. Fu, Multi-scale defects in powder-based additively manufactured metals and alloys, J. Mater. Sci. Technol. 122 (2022) 165–199.
[26] S. Mooraj, J. Dong, K.Y. Xie, W. Chen, Formation of printing defects and their effects on mechanical properties of additively manufactured metal alloys, J. Appl. Phys. 132 (2022), 225108.
[27] Y. Lu, Y. Dong, S. Guo, L. Jiang, H. Kang, T. Wang, B. Wen, Z. Wang, J. Jie, Z. Cao, A promising new class of high-temperature alloys: eutectic high-entropy alloys, Sci. Rep. 4 (2014) 6200.
[28] T. Bhattacharjee, I.S. Wani, S. Sheikh, I.T. Clark, T. Okawa, S. Guo, P. P. Bhattacharjee, N. Tsuji, Simultaneous strength-ductility enhancement of a nano-lamellar AlCoCrFeNi 2.1 eutectic high entropy alloy by cryo-rolling and annealing, Sci. Rep. 8 (2018) 3276.
[29] M. Wang, Y. Lu, T. Wang, C. Zhang, Z. Cao, T. Li, P.K. Liaw, A novel bulk eutectic high-entropy alloy with outstanding as-cast specific yield strengths at elevated temperatures, Scr. Mater. 204 (2021), 114132.
[30] J. Miao, H. Liang, A. Zhang, J. He, J. Meng, Y. Lu, Tribological behavior of an AlCoCrFeNi2.1 eutectic high entropy alloy sliding against different counterfaces, Tribol. Int. 153 (2021), 106599.
[31] M. Wang, Y. Lu, J. Lan, T. Wang, C. Zhang, Z. Cao, T. Li, P.K. Liaw, Lightweight, ultrastrong and high thermal-stable eutectic high-entropy alloys for elevated-temperature applications, Acta Mater. 248 (2023), 118806.
[32] Y. Zhu, S. Zhou, Z. Xiong, Y.J. Liang, Y. Xue, L. Wang, Enabling stronger eutectic high-entropy alloys with larger ductility by 3D printed directional lamellae, Addit. Manuf. 39 (2021), 101901.
[33] Z. Geng, C. Chen, R. Li, J. Luo, K. Zhou, Composition inhomogeneity reduces cracking susceptibility in additively manufactured AlCoCrFeNi2.1 eutectic high-entropy alloy produced by laser powder bed fusion, Addit. Manuf. 56 (2022), 102941.
[34] Y. Guo, H. Su, H. Zhou, Z. Shen, Y. Liu, J. Zhang, L. Liu, H. Fu, Unique strength-ductility balance of AlCoCrFeNi2.1 eutectic high entropy alloy with ultra-fine duplex microstructure prepared by selective laser melting, J. Mater. Sci. Technol. 111 (2022) 298–306.
[35] J. Ren, Y. Zhang, D. Zhao, Y. Chen, S. Guan, Y. Liu, L. Liu, S. Peng, F. Kong, J. D. Poplawsky, G. Gao, T. Voisin, K. An, Y.M. Wang, K.Y. Xie, T. Zhu, W. Chen, Strong yet ductile nanolamellar high-entropy alloys by additive manufacturing, Nature 608 (2022) 62–68.
[36] F. Yang, L. Wang, Z. Wang, Q. Wu, K. Zhou, X. Lin, W. Huang, Ultra strong and ductile eutectic high entropy alloy fabricated by selective laser melting, J. Mater. Sci. Technol. 106 (2022) 128–132.
[37] K. Zhou, J. Li, Q. Wu, Z. Zhang, Z. Wang, J. Wang, Remelting induced fully-equiaxed microstructures with anomalous eutectics in the additive manufactured Ni32Co30Cr10Fe10Al18 eutectic high-entropy alloy, Scr. Mater. 201 (2021), 113952.
[38] W. Jiao, T. Li, X. Chang, Y. Lu, G. Yin, Z. Cao, T. Li, A novel Co-free Al0.75CrFeNi eutectic high entropy alloy with superior mechanical properties, J. Alloy. Compd. 902 (2022), 163814.
[39] D. Vogiatzief, A. Evirgen, S. Gein, V.R. Molina, A. Weisheit, M. Pedersen, Laser powder bed fusion and heat treatment of an AlCrFe2Ni2 high entropy alloy, Front. Mater 7 (2020).
[40] Q. Wu, Z. Wang, X. Hu, T. Zheng, Z. Yang, F. He, J. Li, J. Wang, Uncovering the eutectics design by machine learning in the Al–Co–Cr–Fe–Ni high entropy system, Acta Mater. 182 (2020) 278–286.
[41] B.H. Toby, R.B. Von Dreele, GSAS-II: the genesis of a modern open-source all purpose crystallography software package, J. Appl. Crystallogr. 46 (2013) 544–549.
[42] T. DebRoy, T. Mukherjee, H.L. Wei, J.W. Elmer, J.O. Milewski, Metallurgy, mechanistic models and machine learning in metal printing, Nat. Rev. Mater. 6 (2021) 48–68.
[43] X. Gao, Y. Lu, B. Zhang, N. Liang, G. Wu, G. Sha, J. Liu, Y. Zhao, Microstructural origins of high strength and high ductility in an AlCoCrFeNi2. 1 eutectic high-entropy alloy, Acta Mater. 141 (2017) 59–66.
[44] T. Xiong, S. Zheng, J. Pang, X. Ma, High-strength and high-ductility AlCoCrFeNi2. 1 eutectic high-entropy alloy achieved via precipitation strengthening in a heterogeneous structure, Scr. Mater. 186 (2020) 336–340.
[45] R.E. Smallman, A.H.W. Ngan, Chapter 10-Surfaces, Grain Boundaries and Interfaces, Mod. Phys. Metall. Eighth Ed. Edn Butterworth-Heinemann Oxf, 2014, pp. 415–442.
[46] H. Huang, Y. Wu, J. He, H. Wang, X. Liu, K. An, W. Wu, Z. Lu, Phase-transformation ductilization of brittle high-entropy alloys via metastability engineering, Adv. Mater. 29 (2017), 1701678.
[47] Y. Wu, W.H. Liu, X.L. Wang, D. Ma, A.D. Stoica, T.G. Nieh, Z.B. He, Z.P. Lu, *In-situ* neutron diffraction study of deformation behavior of a multi-component high-entropy alloy, Appl. Phys. Lett. 104 (2014), 051910.
[48] W. Chen, T. Voisin, Y. Zhang, J.B. Forien, C.M. Spadaccini, D.L. McDowell, T. Zhu, Y.M. Wang, Microscale residual stresses in additively manufactured stainless steel, Nat. Commun. 10 (2019) 4338.
[49] D. Yu, K. An, Y. Chen, X. Chen, Revealing the cyclic hardening mechanism of an austenitic stainless steel by real-time *in situ* neutron diffraction, Scr. Mater. 89 (2014) 45–48.
[50] L. Ma, L. Wang, Z. Nie, F. Wang, Y. Xue, J. Zhou, T. Cao, Y. Wang, Y. Ren, Reversible deformation-induced martensitic transformation in Al0. 6CoCrFeNi high-entropy alloy investigated by *in situ* synchrotron-based high-energy X-ray diffraction, Acta Mater. 128 (2017) 12–21.
[51] D. Yu, L. Huang, Y. Chen, P. Komolwit, K. An, Real-time *in situ* neutron diffraction investigation of phase-specific load sharing in a cold-rolled TRIP sheet steel, JOM 70 (2018) 1576–1586.
[52] R. Feng, Y. Rao, C. Liu, X. Xie, D. Yu, Y. Chen, M. Ghazisaeidi, T. Ungar, H. Wang, K. An, Enhancing fatigue life by ductile-transformable multicomponent B2 precipitates in a high-entropy alloy, Nat. Commun. 12 (2021) 3588.
[53] P. Shi, R. Li, Y. Li, Y. Wen, Y. Zhong, W. Ren, Z. Shen, T. Zheng, J. Peng, X. Liang, P. Hu, N. Min, Y. Zhang, Y. Ren, P.K. Liaw, D. Raabe, Y. Wang, Hierarchical crack buffering triples ductility in eutectic herringbone high-entropy alloys, Science 373 (2021) 912–918.
[54] K.M. Bertsch, G. Meric de Bellefon, B. Kuehl, D.J. Thoma, Origin of dislocation structures in an additively manufactured austenitic stainless steel 316L, Acta Mater. 199 (2020) 19–33.
[55] G.K. Williamson, W.H. Hall, X-ray line broadening from filed aluminium and wolfram, Acta Metall. 1 (1953) 22–31.
[56] W. Woo, T. Ungár, Z. Feng, E. Kenik, B. Clausen, X-ray and neutron diffraction measurements of dislocation density and subgrain size in a friction-stir-welded aluminum alloy, Metall. Mater. Trans. A. 41 (2010) 1210–1216.
[57] B.E. Warren, X-ray Diffraction, Dover Publications, 1990.
[58] Q. Xie, Y. Chen, P. Yang, Z. Zhao, Y.D. Wang, K. An, *In-situ* neutron diffraction investigation on twinning/detwinning activities during tension-compression load reversal in a twinning induced plasticity steel, Scr. Mater. 150 (2018) 168–172.
[59] M. Naeem, H. He, F. Zhang, H. Huang, S. Harjo, T. Kawasaki, B. Wang, S. Lan, Z. Wu, F. Wang, Y. Wu, Z. Lu, Z. Zhang, C.T. Liu, X.L. Wang, Cooperative deformation in high-entropy alloys at ultralow temperatures, Sci. Adv. 6 (2020) eaax4002.
[60] B.E. Warren, X-ray studies of deformed metals, Progr Met. Phys. 8 (1959).
[61] B. Cai, B. Liu, S. Kabra, Y. Wang, K. Yan, P.D. Lee, Y. Liu, Deformation mechanisms of Mo alloyed FeCoCrNi high entropy alloy: *in situ* neutron diffraction, Acta Mater. 127 (2017) 471–480.
[62] F. Wang, G.H. Balbus, S. Xu, Y. Su, J. Shin, P.F. Rottmann, K.E. Knipling, J. C. Stinville, L.H. Mills, O.N. Senkov, I.J. Beyerlein, T.M. Pollock, D.S. Gianola, Multiplicity of dislocation pathways in a refractory multiprincipal element alloy, Science 370 (2020) 95–101.
[63] J. Wang, Q. Zhou, S. Shao, A. Misra, Strength and plasticity of nanolaminated materials, Mater. Res. Lett. 5 (2017) 1–19.

[64] J.Y. He, H. Wang, H.L. Huang, X.D. Xu, M.W. Chen, Y. Wu, X.J. Liu, T.G. Nieh, K. An, Z.P. Lu, A precipitation-hardened high-entropy alloy with outstanding tensile properties, Acta Mater 102 (2016) 187–196.
[65] E.O. Hall, The deformation and ageing of mild steel: III discussion of results, Proc. Phys. Soc. Sect. B. 64 (1951) 747–753.
[66] N.J. Petch, The cleavage strength of polycrystals, J. Iron Steel Inst. 174 (1953) 25–28.
[67] Y.Y. Zhao, Z.F. Lei, Z.P. Lu, J.C. Huang, T.G. Nieh, A simplified model connecting lattice distortion with friction stress of Nb-based equiatomic high-entropy alloys, Mater. Res. Lett. 7 (2019) 340–346.
[68] S.S. Sohn, A. Kwiatkowski da Silva, Y. Ikeda, F. Körmann, W. Lu, W.S. Choi, B. Gault, D. Ponge, J. Neugebauer, D. Raabe, Ultrastrong medium-entropy single-phase alloys designed via severe lattice distortion, Adv. Mater. 31 (2019), 1807142.
[69] I. Ondicho, B. Alunda, K. Kamau, Solid solution strengthening in high-entropy alloys, (2022).
[70] C.T. Liu, P.J. Maziasz, Microstructural control and mechanical properties of dual-phase TiAl alloys, Intermetallics 6 (1998) 653–661.
[71] L. Fan, T. Yang, Y. Zhao, J. Luan, G. Zhou, H. Wang, Z. Jiao, C.T. Liu, Ultrahigh strength and ductility in newly developed materials with coherent nanolamellar architectures, Nat. Commun. 11 (2020) 6240.
[72] T.H. Courtney, Mechanical Behavior of Materials, Waveland Press, 2005.
[73] M. Chen, E. Ma, K.J. Hemker, H. Sheng, Y. Wang, X. Cheng, Deformation twinning in nanocrystalline aluminum, Science 300 (2003) 1275–1277.
[74] Q. Pan, L. Zhang, R. Feng, Q. Lu, K. An, A.C. Chuang, J.D. Poplawsky, P.K. Liaw, L. Lu, Gradient-cell–structured high-entropy alloy with exceptional strength and ductility, Science (2021) eabj8114.
[75] D.J. Magagnosc, D.M. Field, C.S. Meredith, K. An, T.R. Walter, K.R. Limmer, J. T. Lloyd, Temperature and stress dependent twinning behavior in a fully austenitic medium-Mn steel, Acta Mater 231 (2022), 117864.
[76] Y.T. Zhu, X.Z. Liao, X.L. Wu, Deformation twinning in nanocrystalline materials, Prog. Mater. Sci. 57 (2012) 1–62.
[77] Q. Wu, F. He, J. Li, H.S. Kim, Z. Wang, J. Wang, Phase-selective recrystallization makes eutectic high-entropy alloys ultra-ductile, Nat. Commun. 13 (2022) 1–8.
[78] A. Das, P.C. Chakraborti, S. Tarafder, H. Bhadeshia, Analysis of deformation induced martensitic transformation in stainless steels, Mater. Sci. Technol. 27 (2011) 366–370.
[79] Y. Yang, T. Chen, L. Tan, J.D. Poplawsky, K. An, Y. Wang, G.D. Samolyuk, K. Littrell, A.R. Lupini, A. Borisevich, Bifunctional nanoprecipitates strengthen and ductilize a medium-entropy alloy, Nature 595 (2021) 245–249.
[80] L. Vitos, Total-energy method based on the exact muffin-tin orbitals theory, Phys. Rev. B. 64 (2001), 014107.
[81] O.K. Andersen, C. Arcangeli, R.W. Tank, T. Saha-Dasgupta, G. Krier, O. Jepsen, I. Dasgupta, Third-generation TB-LMTO, MRS Online Proc. Libr. OPL. 491 (1997) 3.
[82] B.L. Gyorffy, Coherent-potential approximation for a nonoverlapping-muffin-tin-potential model of random substitutional alloys, Phys. Rev. B. 5 (1972) 2382.
[83] J.P. Perdew, K. Burke, M. Ernzerhof, Generalized gradient approximation made simple, Phys. Rev. Lett. 77 (1996) 3865.
[84] W. Li, S. Lu, Q.M. Hu, S.K. Kwon, B. Johansson, L. Vitos, Generalized stacking fault energies of alloys, J. Phys. Condens. Matter 26 (2014), 265005.
[85] Z. Dong, S. Schönecker, W. Li, D. Chen, L. Vitos, Thermal spin fluctuations in CoCrFeMnNi high entropy alloy, Sci. Rep. 8 (2018) 1–7.
[86] B.L. Gyorffy, A.J. Pindor, J. Staunton, G.M. Stocks, H. Winter, A first-principles theory of ferromagnetic phase transitions in metals, J. Phys. F Met. Phys. 15 (1985) 1337.
[87] F. Birch, Finite elastic strain of cubic crystals, Phys. Rev. 71 (1947) 809.
[88] H. Huang, X. Li, Z. Dong, W. Li, S. Huang, D. Meng, X. Lai, T. Liu, S. Zhu, L. Vitos, Critical stress for twinning nucleation in CrCoNi-based medium and high entropy alloys, Acta Mater 149 (2018) 388–396.
[89] J. Ding, Q. Yu, M. Asta, R.O. Ritchie, Tunable stacking fault energies by tailoring local chemical order in CrCoNi medium-entropy alloys, Proc. Natl. Acad. Sci 115 (2018) 8919–8924.
[90] J. Su, D. Raabe, Z. Li, Hierarchical microstructure design to tune the mechanical behavior of an interstitial TRIP-TWIP high-entropy alloy, Acta Mater 163 (2019) 40–54.